Campanyà, J., Ogaya, X., Jones, A. G., Rath, V., Vozar, J., Meqbel, N. (2016): The advantages of complementing MT profiles in 3-D environments with geomagnetic transfer function and interstation horizontal magnetic transfer function data: results from a synthetic case study. - *Geophysical Journal International*, *207*, 3, pp. 1818—1836.

DOI: http://doi.org/10.1093/gji/ggw357

Geophysical Journal International

Geophys. J. Int. (2016) **207,** 1818–1836
Advance Access publication 2016 September 23
GJI Geomagnetism, rock magnetism and palaeomagnetism

doi: 10.1093/gji/ggw357

The advantages of complementing MT profiles in 3-D environments with geomagnetic transfer function and interstation horizontal magnetic transfer function data: results from a synthetic case study

Joan Campanyà,[1] Xènia Ogaya,[1] Alan G. Jones,[1,*] Volker Rath,[1] Jan Vozar[1,†] and Naser Meqbel[2]

[1]*Dublin Institute for Advanced Studies, School of Cosmic Physics, Geophysics section,* 5 *Merrion Square, Dublin* 2, *Ireland. E-mail: campanya@cp.dias.ie*
[2]*German Research Centre For Geosciences, GFZ-Potsdam, Department* 2 *Geophysics, Telegrafenberg, D*-14473 *Potsdam, Germany*

Accepted 2016 September 22. Received 2016 September 20; in original form 2015 June 14; Editorial Decision 2016 September 20

SUMMARY

As a consequence of measuring time variations of the electric and the magnetic field, which are related to current flow and charge distribution, magnetotelluric (MT) data in 2-D and 3-D environments are not only sensitive to the geoelectrical structures below the measuring points but also to any lateral anomalies surrounding the acquisition site. This behaviour complicates the characterization of the electrical resistivity distribution of the subsurface, particularly in complex areas. In this manuscript we assess the main advantages of complementing the standard MT impedance tensor (***Z***) data with interstation horizontal magnetic tensor (***H***) and geomagnetic transfer function (***T***) data in constraining the subsurface in a 3-D environment beneath a MT profile. Our analysis was performed using synthetic responses with added normally distributed and scattered random noise. The sensitivity of each type of data to different resistivity anomalies was evaluated, showing that the degree to which each site and each period is affected by the same anomaly depends on the type of data. A dimensionality analysis, using ***Z***, ***H*** and ***T*** data, identified the presence of the 3-D anomalies close to the profile, suggesting a 3-D approach for recovering the electrical resistivity values of the subsurface. Finally, the capacity for recovering the geoelectrical structures of the subsurface was evaluated by performing joint inversion using different data combinations, quantifying the differences between the true synthetic model and the models from inversion process. Four main improvements were observed when performing joint inversion of ***Z***, ***H*** and ***T*** data: (1) superior precision and accuracy at characterizing the electrical resistivity values of the anomalies below and outside the profile; (2) the potential to recover high electrical resistivity anomalies that are poorly recovered using ***Z*** data alone; (3) improvement in the characterization of the bottom and lateral boundaries of the anomalies with low electrical resistivity; and (4) superior imaging of the horizontal continuity of structures with low electrical resistivity. These advantages offer new opportunities for the MT method by making the results from a MT profile in a 3-D environment more convincing, supporting the possibility of high-resolution studies in 3-D areas without expending a large amount of economical and computational resources, and also offering better resolution of targets with high electrical resistivity.

Key words: Magnetotellurics; Magnetic and electrical properties.

1 INTRODUCTION

Over the last 30 yr theoretical and technological developments have justified and established the use of the magnetotelluric (MT) method in many regions with widely differing objectives, by adjusting it to the specific requirements of each area of study (e.g. Chave & Jones 2012). Thanks to this relatively rapid progress, MT studies have been undertaken from the deepest seas (e.g. Heinson *et al.* 2000; Baba *et al.* 2006; Seama *et al.* 2007) to the highest mountain ranges on Earth (e.g. Le Pape *et al.* 2012; Kühn *et al.* 2014), characterizing the geoelectrical subsurface in a large variety of regions and for both academic and commercial applications (e.g. Heinson *et al.* 2006; Falgàs *et al.* 2009; Jones *et al.* 2009; Tuncer *et al.* 2009;

*Now at: Complete MT Solutions, Ottawa, Canada.
†Now at: Earth Science Institute of the Slovak Academy of Sciences, Geophysical Division, Dubravska cesta 9, 84005 Bratislava, Slovakia.

Campanyà *et al.* 2011; La Terra & Menezes 2012; Ogaya *et al.* 2014; Piña-Varas *et al.* 2014). However, limitations of the MT method still exist and there is ample room for improvement.

One of the main issues hindering high resolution of the subsurface using MT is that in 3-D environments the data can be strongly affected by geoelectrical structures located some distance away from the sites where the data are acquired, affecting most data sets to at least some degree (e.g. Brasse *et al.* 2002), and potentially leading to inaccurate characterization of the subsurface below the study area (e.g. Jones & Garcia 2003). In recent years, the availability of 3-D forward and inversion codes (e.g. Farquharson *et al.* 2002; Siripunvaraporn *et al.* 2005a; Avdeev & Avdeeva 2009; Egbert & Kelbert 2012; Kelbert *et al.* 2014; Grayver 2015; Usui 2015) has improved the characterization of the subsurface in these situations, and 3-D inversion has become a more routine procedure for the EM community, although more experience is needed before it becomes as firmly established as is 2-D inversion (e.g. Miensopust *et al.* 2013; Tietze & Ritter 2013; Kiyan *et al.* 2014).

However, difficulties associated with logistics, acquisition costs and instrumentation availability still often require MT field specialists to acquire data predominantly along 2-D profiles, even when the study is performed in a 3-D environment. Jones (1983), Wanamaker *et al.* (1984), Berdichevsky *et al.* (1998), Park & Mackie (2000), Ledo *et al.* (2002) and Ledo (2005) studied the limitations of 2-D interpretation of 3-D MT data and made various recommendations, showing some situations where 2-D inversion of 3-D data can properly reproduce the geoelectrical subsurface when the content in the 2-D modes is appropriately chosen for inversion. Siripunvaraporn *et al.* (2005b) suggest that if the data are 3-D in nature but collected along a profile rather than on a grid, the results from the 3-D inversion of the MT profile are superior to the results obtained by performing 2-D inversion of the same data, even with the far coarser mesh employed in 3-D as compared to 2-D inversion. Following this idea, several publications recommend inverting all four components of the MT impedance tensor (***Z***), for example Siripunvaraporn *et al.* (2005b), Tietze & Ritter (2013) and Kiyan *et al.* (2014), instead of the approach of inverting only the off-diagonal components ($\boldsymbol{Z}_o$) (e.g. Sasaki 2004; Sasaki & Meju 2006). However, the presence of anthropogenic noise can strongly reduce the quality of the ***Z*** data, in particular the quality of the diagonal components, making it sometimes worthless to use all components of the ***Z*** tensor for the inversion process because of scatter and/or extremely large errors in the diagonal components of ***Z***.

Interstation horizontal magnetic transfer function (***H***) and the geomagnetic transfer function (***T***) data, which are not affected by electric field effects caused by galvanic distortion from charges on conductivity boundaries or gradients on small-scale structures, have been used to improve MT results and constrain the subsurface using 2-D or 3-D inversion (e.g. Soyer & Brasse 2001, 2-D ***H*** only of field data; Gabàs & Marcuello 2003, 2-D $\boldsymbol{Z} + \boldsymbol{T}$ theoretical study; Siripunvaraporn & Egbert 2009, 3-D ***Z***, ***T*** and $\boldsymbol{Z} + \boldsymbol{T}$ of synthetic and field data; Berdichevsky *et al.* 2010a, 2-D $\boldsymbol{Z} + \boldsymbol{T}$ of field data; Habibian *et al.* 2010, 2-D $\boldsymbol{Z} + \boldsymbol{T}$ of field data; Tietze & Ritter 2013), 3-D ***Z***, ***T*** and $\boldsymbol{Z} + \boldsymbol{T}$ of synthetic and field data, (Habibian & Oskooi 2014, 2-D ***H*** *cf.* ***T*** theoretical study, Meqbel *et al.* 2014, ***Z***, ***T*** and $\boldsymbol{Z} + \boldsymbol{T}$ of field data, Rao *et al.* 2014, ***Z*** and $\boldsymbol{Z} + \boldsymbol{T}$ of field data; Yang *et al.* 2015, ***Z*** and $\boldsymbol{Z} + \boldsymbol{T}$ of field data; Varentsov 2015a,b, performing 2-D, 2-D+ and quasi 3-D inversion using ***Z***, ***T*** and ***H*** with theoretical and field data), but no-one has yet undertaken an examination of the advantages of including ***H*** and ***T***, simultaneously, when performing 3-D inversion of ***Z*** data ($\boldsymbol{Z} + \boldsymbol{H} + \boldsymbol{T}$ in 3-D). It should be noted that the magnetic effects caused by galvanic distortion charges do affect ***Z***, ***H*** and ***T*** (e.g. Chave & Smith 1994; Chave & Jones 1997), however, these effects rapidly decrease with increasing period due to the square root dependence of their sensitivity on frequency, and can effectively be ignored over broad frequency bands. This rapid decrease is true for pure galvanic distortion but not in other situations as for example in the case of presence of current channelling caused by thin-long structures (e.g. Lezaeta & Haak 2003; Campanyà *et al.* 2012).

Another area for improvement for the MT geophysical technique is its issue with recovering high electrical resistivity anomalies in areas with contrasting low electrical resistivity values, or areas beneath strong low resistivity anomalies (e.g. Vozoff 1991; Berdichevsky *et al.* 1998; Bedrosian 2007; Berdichevsky & Dmitriev 2008; Chave & Jones 2012; Miensopust *et al.* 2013). The capacity at recovering low electrical resistivity structures is a particular strength of the MT method as a geophysical technique when characterizing geoelectrical structures from the first few metres to the asthenosphere (e.g. Jones 1999; Ledo *et al.* 2011; Rosell *et al.* 2011; Campanyà *et al.* 2012; Ogaya *et al.* 2013; Dong *et al.* 2014; Muñoz 2014). However, issues in recovering high electrical resistivity anomalies are somewhat of a limitation for the MT method in certain resource exploration applications, for example where resistive hydrocarbons are present (e.g. Simpson & Bahr 2005; Unsworth 2005) and very high quality data are required.

The aim of this paper is to evaluate and highlight, from numerical experiments, the advantages in combining ***Z*** (full tensor) or $\boldsymbol{Z}_o$ (off-diagonal components only) responses with ***H*** and ***T*** responses when characterizing and modelling the subsurface below a MT profile in a 3-D environment, and to evaluate if the sensitivity and resolution issues discussed above can be addressed.

2 EXPERIMENTAL DESIGN

The numerical experiment consisted of calculating the forward responses of a defined synthetic model with embedded 3-D anomalies. These responses were used for a sensitivity test, evaluating the effects of each anomaly on the different types of data, ***Z*** or $\boldsymbol{Z}_o$, ***H*** and ***T***. Dimensionality analyses and inversions were also performed characterizing the 3-D behaviour of the responses and recovering the electrical resistivity structures of the subsurface by performing 3-D joint inversion with different combinations of ***Z***, ***H*** and ***T***. The fit of the data and the accuracy for recovering the electrical resistivity distribution of the subsurface was quantified with the aim of providing a robust support to the conclusions extracted from the experiment.

2.1 Synthetic model

The background structure of the synthetic model (Fig. 1) is a 1-D layered Earth comprised of four layers: (1) a resistivity of 100 Ωm between 0 m (the surface) and 90 m depth; (2) a resistivity of 400 Ωm between 90 and 1500 m depth; (3) a low-resistive layer of 10 Ωm between 1500 and 2000 m depth; and (4) a layer from 2000 to 90 km depth with a resistivity of 200 Ωm. A half-space of 20 Ωm at 90 km depth was added at the bottom of the model to ensure that the EM fields at the adopted periods do not penetrate away from the utilized mesh, also creating a more common response for the longest periods simulating the existence of a hypothetical asthenosphere. This 1-D layered background was used to simulate a more realistic and complex situation than a homogeneous background, and at the same time to highlight the inherent deficiencies of ***H*** and ***T*** data for resolving laterally uniform structures.

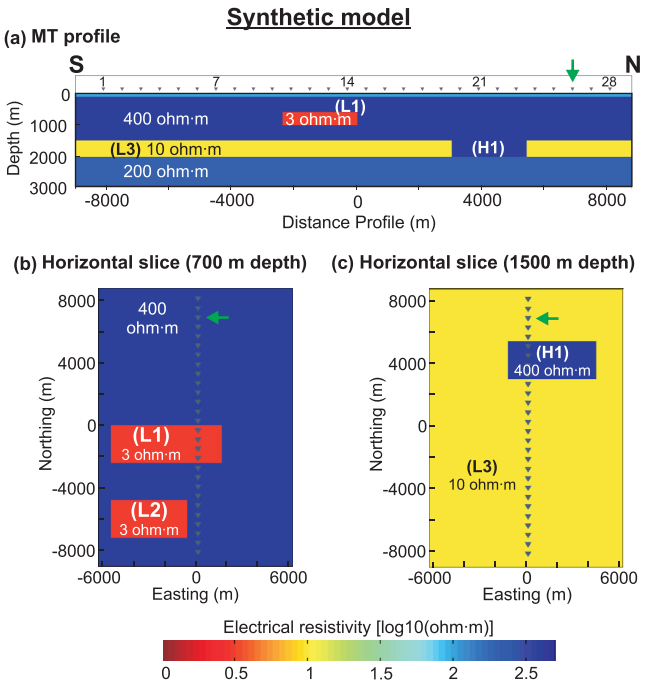

Figure 1. Synthetic geoelectrical model composed of four layers: (1) Between 0 and 90 m depth with an electrical resistivity of 100 Ωm; (2) Between 90 and 1500 m depth with an electrical resistivity of 400 Ωm; (3) Between 1500 and 2000 m depth with an electrical resistivity of 10 Ωm; (4) Layer from 2000 m to 90 km depth with an electrical resistivity of 200 Ωm. Two low electrical resistivity structures (L1 and L2) and a high electrical resistivity body (H1) are also present. L1 and L2 are located between 500 and 1000 m depth and have an electrical resistivity value of 3 Ωm. H1 is located between 1500 and 2000 m depth with electrical resistivity values of 400 Ωm. The green arrows points to site 26, which is used as a neighbouring reference site for $\boldsymbol{H}$ responses.

Within this layered background structure there are three 3-D resistivity bodies; two low resistivity structures (L1 and L2) and a high resistivity body (H1; Fig. 1). Both low and high resistivity anomalies have been added to highlight the resolution differences between these two types of anomalies when characterizing the subsurface. L1 and L2 are located between 500 and 1000 m depth and have a resistivity value of 3 Ωm. H1 is located between 1500 and 2000 m depth, with a resistivity value of 400 Ωm. L1 and H1 cross the single north–south MT profile whereas the L2 structure lies completely outside the simulated linear acquisition profile to its west; this geometry was chosen with the aim of evaluating the capacity of the various inversions in determining structures outside the profile and to appraise if unexpected artefacts associated with L2 may be artificially created below the profile. Due to the importance of the role of $\boldsymbol{H}$ and $\boldsymbol{T}$ responses in characterizing the conducting 10 Ωm layer between 1500 and 2000 m depth, this layer has been labelled as target body L3.

The forward response of the synthetic model at the 28 sites located along the north–south profile, covering a range of periods between 0.0001 and 1000 s (frequencies of 10 000–0.001 Hz), was calculated using the ModEM code (Egbert & Kelbert 2012; Kelbert *et al.* 2014), modified for inclusion on $\boldsymbol{H}$ responses (see Fig. S1, for more details), with a large 3-D mesh that comprised 222 × 182 × 132 cells in the north–south, east–west and vertical directions, respectively. The core of the mesh comprised 162 × 112 × 132 cells with a horizontal cell size of 120 m × 120 m, while the distance between sites was 600 m. The lateral size of the padding cells increased by a factor of 1.3 from the edges of the core outward to the boundaries. The thickness of the top layer was 10 m, with an increasing factor of 1.048 for the subsequent layers in the z-direction, ensuring that the thickness of each cell within the depth of interest, namely the first 3 km, is smaller than the horizontal cell size.

2.2 Response types

As mentioned above, three different EM tensor relationships were studied in our numerical experiment: (1) the standard MT impedance tensor ($\boldsymbol{Z}$) (eq. 1); (2) the geomagnetic transfer function ($\boldsymbol{T}$) (eq. 2) and (3) the interstation horizontal magnetic transfer function ($\boldsymbol{H}$) (eq. 3).

$$\boldsymbol{e}_l = \boldsymbol{Z}\boldsymbol{h}_l \tag{1}$$

$$h_z^l = \boldsymbol{T}\boldsymbol{h}_l \tag{2}$$

$$\boldsymbol{h}_l = \boldsymbol{H}_{ln}\,\boldsymbol{h}_n, \tag{3}$$

where $\boldsymbol{h}_l$ and $\boldsymbol{h}_n$ are two component vectors comprising the horizontal magnetic components at the local site l $[h_x^l, h_y^l]$ and the neighbouring reference site n $[h_x^n, h_y^n]$, respectively. The neighbouring reference site is the site used to relate the horizontal magnetic fields of all the studied sites (local sites) with the horizontal magnetic fields of this site (neighbouring reference site). $\boldsymbol{e}_l$ is a two component vector comprising the horizontal electric components at the local site l $[e_x^l, e_y^l]$ and h_z^l is the vertical component of the magnetic field recorded at the local site l. $\boldsymbol{Z}$ and $\boldsymbol{H}_{ln}$ are 2 × 2 complex matrices and $\boldsymbol{T}$ is a 1 × 2 complex vector. In all cases dependence on frequency is assumed.

The $\boldsymbol{H}$ transfer function relates the horizontal magnetic field between two different sites (one of the local sites and the neighbouring reference site), characterizing the differences associated with the electrical resistivity distribution below the two sites. This requires that the structures below the neighbouring reference site should also be characterized (e.g. Soyer 2002), which can be achieved by having the neighbouring reference site within the area of study.

Note that, in case the neighbouring reference site used to acquire and process the data is outside the study area, for the inversion process the $\boldsymbol{H}$ data can be rearranged using as a neighbouring reference site any of the sites in the study area, even if the data at this site were not acquired during the whole survey. This can be achieved following steps analogous to the ones used in the ELICIT methodology to process MT data (Campanyà *et al.* 2014), in which inputs and outputs related by the transfer functions do not need to be acquired simultaneously.

For the experiment presented in this paper, site 26 (identified with a green arrow in Fig. 1) has been chosen as a neighbouring reference site for all of the $\boldsymbol{H}$ responses as there are no prescribed anomalies below it and thereby facilitating simple evaluation of the properties of the $\boldsymbol{H}$ responses.

2.3 Sensitivity analysis

A non-linear sensitivity test was performed to identify the sites and periods responsive to the geoelectrical anomalies and to characterize and quantify the effects of those anomalies on the $\boldsymbol{Z}$, $\boldsymbol{H}$ and $\boldsymbol{T}$ responses, individually and collectively. The sensitivity test consisted of calculating the differences between the forward responses of the 1-D layered model with the studied anomalies included (L1, L2 and H1) and the forward responses of the background 1-D layered

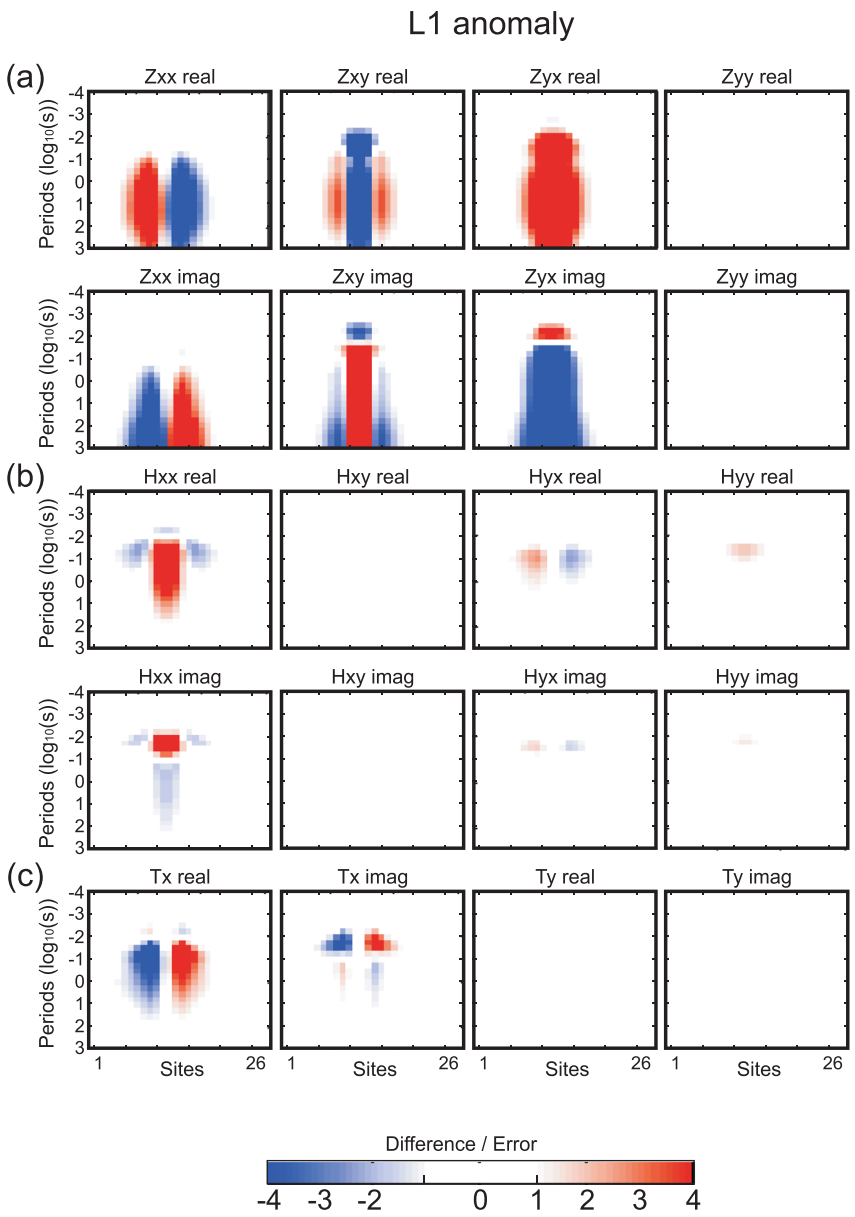

Figure 2. Results of the sensitivity test for the L1 anomaly. Values obtained by calculating the differences between the forward responses of the 1-D layered model containing L1 anomaly and the forward responses of the background 1-D layered model without anomalies. The differences are divided by the assumed error, thus showing how sensitive the responses are to the anomaly with respect to the errors. White areas are periods that are non-sensitive to L1 (differences smaller than the assumed error). Red and blue areas are periods that are sensitive to L1.

model without any anomalies. The differences between the model responses were divided by the adopted error, thus highlighting how sensitive the responses are to the anomalies with respect to the errors in the data. Impedance error bounds were set to 5 per cent of $|Zij|$ for diagonal and off-diagonal impedance tensor elements, in combination with an error floor of 5 per cent of $|Z_{xy} * Z_{yx}|^{\frac{1}{2}}$ for the diagonal elements. Error floor was added to avoid the extremely small error values associated with the periods of the *Zxx* and *Zyy* components not affected by the 3-D anomalies. For the **T** and the **H** responses we used constant error bounds of 0.02. These errors were chosen consistent with the errors assumed in other publications with both real and synthetic data (e.g. Soyer 2002; Habibian *et al.* 2010; Egbert & Kelbert 2012; Tietze & Ritter 2013). Figs 2–5 show the effects of the L1, L2, H1 and L1 + L2 + H1 anomalies, respectively, individually and collectively as contoured pseudo-sections, with distance along the profile on the abscissa and period, on a decadic logarithm scale, along the ordinate. Differences within the assumed errors, values between −1 and 1, are white in colour and show the periods for the various components at the sites that are insensitive to the anomalies. Therefore, for these periods the anomalies cannot be resolved within the assumed precision. Dark blue and dark red areas show periods at the sites that are highly sensitive to the anomaly, with anomalous responses of four or more standard deviations of the assumed errors. Note the somewhat simplicity of anomalous response for single features (Figs 2–4), but the complexity of the response when all features are included (Fig. 5). The total summed effect of each anomaly on the responses is quantified in Fig. 6. In this figure, the sensitivities of $\boldsymbol{Z}_o$ (off-diagonal components of $\boldsymbol{Z}$) are also shown, as the off-diagonal components have been often used as a data type, although most practitioners now invert the full impedance tensor $\boldsymbol{Z}$.

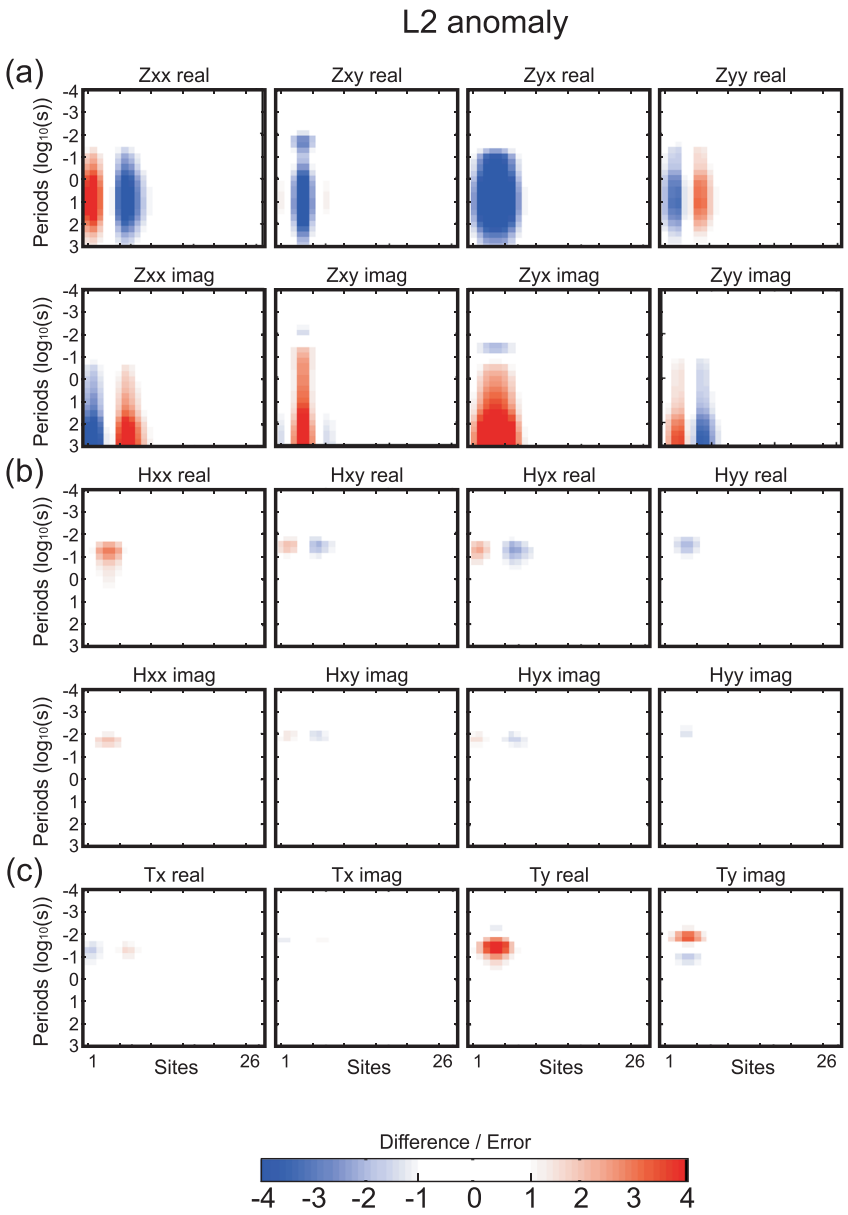

Figure 3. Results of the sensitivity test for the L2 anomaly. Values obtained by calculating the differences between the forward responses of the 1-D layered model containing L2 anomaly and the forward responses of the background 1-D layered model without anomalies. The differences are divided by the assumed error, thus showing how sensitive the responses are to the anomaly with respect to the errors. White areas are periods that are non-sensitive to L2 (differences smaller than the assumed error). Red and blue areas are periods that are sensitive to L2.

These pseudo-sections show the sensitivity of each period at each site, with respect to the adopted error, between the responses of the 1-D layered model with the studied anomaly and the responses of the 1-D layered model without any anomaly. The sensitivity values for each period and site were calculated following eq. (4):

$$S = 1 + \sum \left(abs \left[\frac{model\ response - data}{error} \right] - 1 \right) \quad \forall \frac{model\ response - data}{error} > 1, \tag{4}$$

where S is the sensitivity per each period and site. Note that this equation has the condition that each component of the analysed tensor relationship, for each period and site, is included in the summand only if difference between model response and data is greater than the assumed error, which means is sensitive to the analysed anomaly.

Four main conclusions can be drawn from the sensitivity tests:

(1) The influence of each anomaly at a given site and at a given period depends upon the types of responses used. Whereas the ***Z*** and ***H*** responses are more sensitive at the sites directly above the anomalies, the ***T*** responses are more sensitive at the sites located at the edge of the anomalies. This can be understood as a consequence of the physics of induction. For a uniform source field there is no vertical field above a laterally uniform Earth, the greatest effects in ***T*** are off to the side of the anomaly (see e.g. Jones 1986).

(2) The anomalies affect a narrower range of periods for ***H*** and ***T*** responses than for ***Z*** responses. For the ***Z*** responses, the anomalous effect extends to longer periods without seeing the end of the effect of the anomalies for the analysed periods. This is because

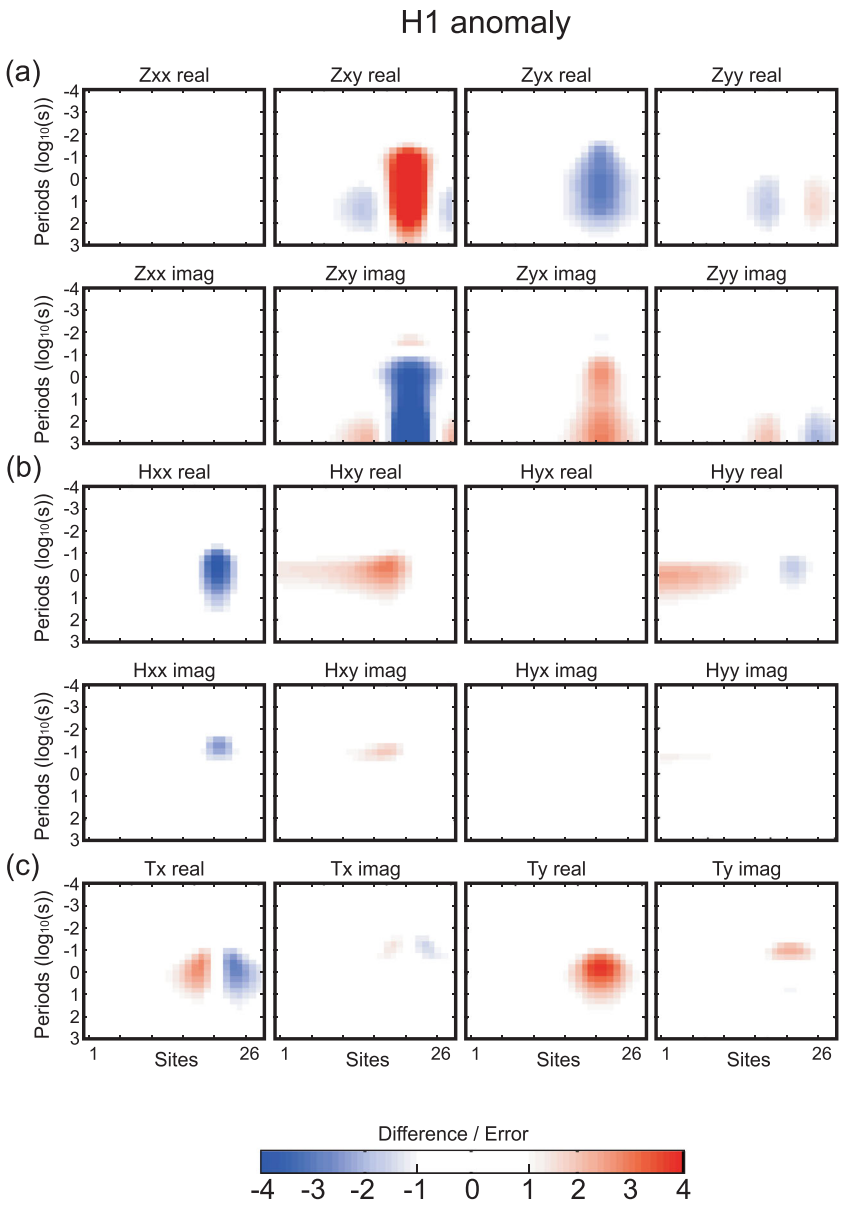

Figure 4. Results of the sensitivity test for the H1 anomaly. Values obtained by calculating the differences between the forward responses of the 1-D layered model containing H1 anomaly and the forward responses of the background 1-D layered model without anomalies. The differences are divided by the assumed error, thus showing how sensitive the responses are to the anomaly with respect to the errors. White areas are periods that are non-sensitive to H1 (differences smaller than the assumed error). Red and blue areas are periods that are sensitive to H1.

the galvanic charges on the boundaries of conductivity contrasts, once imposed, remain in place at all longer periods. There are both magnetic and electric effects of the charges (see e.g. Chave & Smith 1994; Chave & Jones 1997; Jones 2012) but the magnetic effects drop off very quickly with increasing period for isolated anomalies.

(3) For the ***H*** and ***T*** responses the influence of anomaly L1 is stronger than for anomalies L2 and H1, though the difference is not as large as for ***Z*** and $\boldsymbol{Z}_o$ responses (Fig. 6). This is because MT is primarily sensitive to elongated conductors, and in our numerical experiment L1 is the longest and most conducting of the three anomalies. This could result in the inversion modelling of the $\boldsymbol{Z}_o$ and ***Z*** responses naturally focussing more on fitting data responding to the L1 structure than to the other anomalies, as this will lead to the greatest overall misfit reduction, whereas for the ***H*** and ***T*** responses the L1, L2 and H1 anomalies will have similar weight during the inversion process.

(4) With the 3-D geoelectrical structures (L1, L2 and H1) orientated perpendicular to the MT profile, the presence of sensitive periods for the Z_{xx}, Z_{yy}, H_{xy}, H_{yx}, H_{yy} and T_y components implies that the analysed responses are sensitive to the 3-D nature of the anomalies (Berdichevsky & Dmitriev 2008). However, in this numerical experiment, the effect of the L1 anomaly on the *y* component of the ***T*** responses is smaller than the assumed error (Fig. 2c), which means that in this situation the ***T*** responses 'see' the L1 anomaly as a 2-D structure within the precision of the responses.

The different influences of each anomaly in relation to the examined types of responses suggest that the use of ***H*** and ***T*** responses as

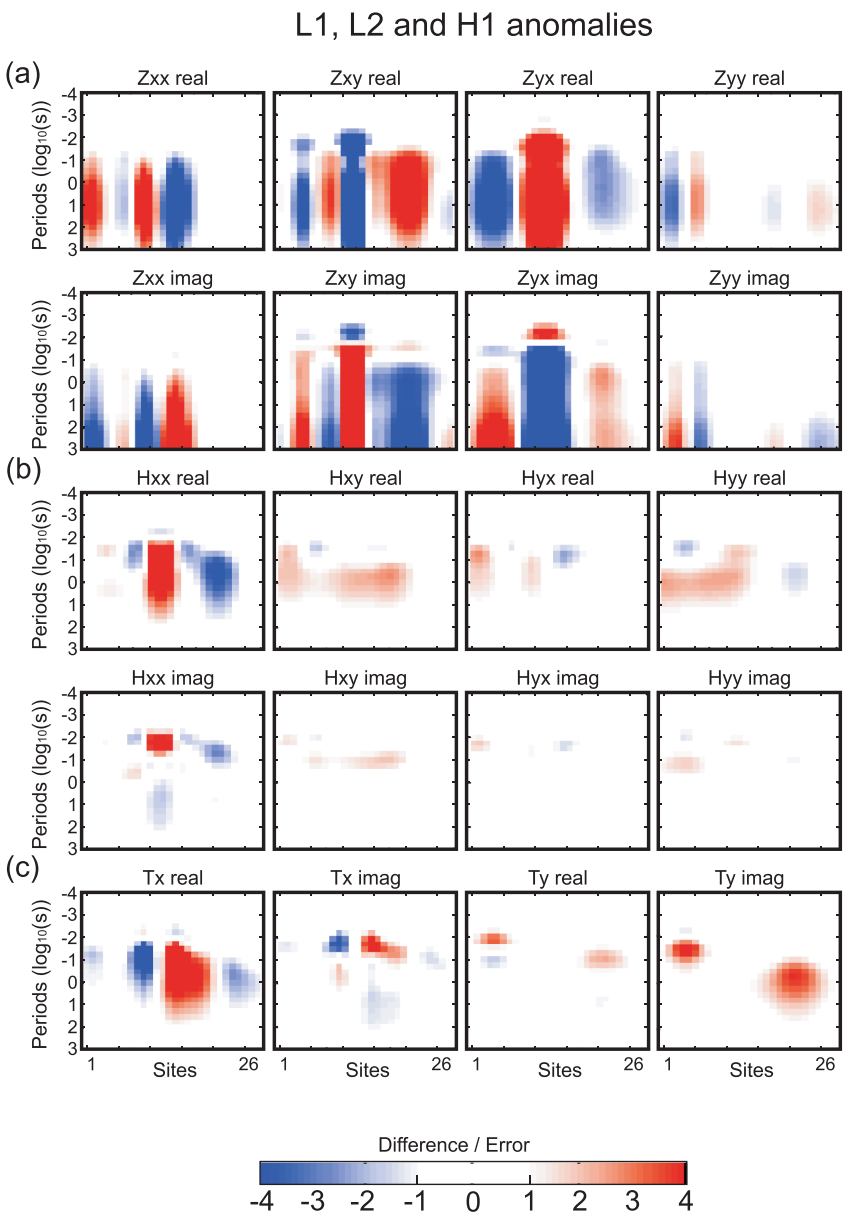

Figure 5. Results of the sensitivity test for the combined L1 + L2 + H1 anomalies. Values obtained by calculating the differences between the forward responses of the 1-D layered model containing L1 + L2 + H1 anomalies and the forward responses of the background 1-D layered model without anomalies. The differences are divided by the assumed error, thus showing how sensitive the responses are to the anomalies with respect to the errors. White areas are periods that are non-sensitive to L1 + L2 + H1 anomalies (differences smaller than the assumed error). Red and blue areas are periods that are sensitive to L1 + L2 + H1.

an accompaniment to the commonly used $\boldsymbol{Z}_o$ and $\boldsymbol{Z}$ responses will introduce complementary information that enhances resolution and restricts acceptable model space, whilst simultaneously increasing the weight to the L2 and H1 anomalies during the inversion process.

2.4 Dimensionality analysis

The dimensionality of the synthetic model was analysed using the $\boldsymbol{Z}$, $\boldsymbol{H}$ and $\boldsymbol{T}$ responses separately (Fig. 7). Normally distributed scattered random noise was added to the responses in a manner consistent with the errors assumed for the sensitivity test. In particular, the added noise at each site and frequency was derived by generating random numbers from the normal distribution with mean parameter (0) and standard deviation (1) and multiplying this number by the data error of the responses. The same errors as those assumed for the sensitivity test were assumed for the distorted responses.

For the $\boldsymbol{Z}$ responses, dimensionality analysis was performed using the phase tensor (Caldwell *et al.* 2004), as this method is routinely used for evaluating the dimensionality of the study area without being affected by galvanic distortion. To assess the presence of 3-D structures, a variant of the β criterion was used. Typically β is used to justify 2-D/3-D interpretation based on a threshold value (see e.g. Caldwell *et al.* 2004; Thiel *et al.* 2009; Booker 2014). In this case we took into account the errors of the data, as suggested by Booker (2014), interpreting all deviations from zero that are above the error in determining β as a 3-D. The ellipses are each filled with a colour associated with the magnitude of β divided by this error. Values

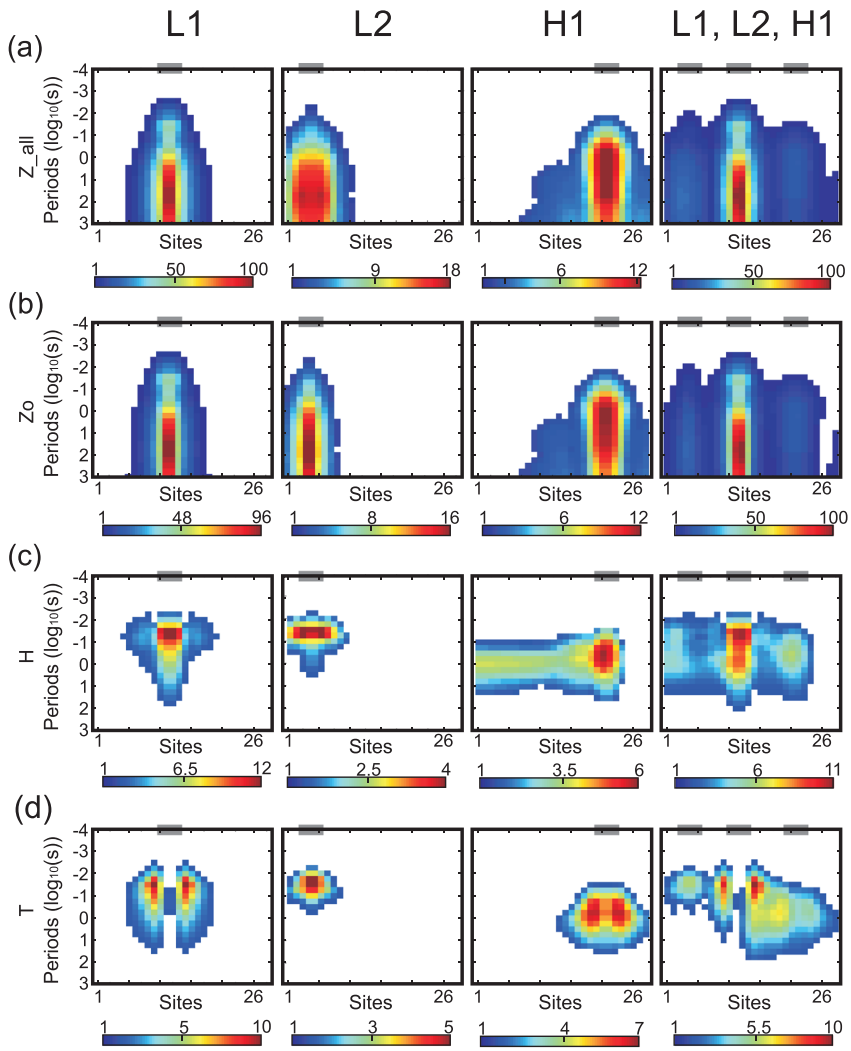

Figure 6. Results from the sensitivity test to quantify the effect of each anomaly on the ***Z***, $\boldsymbol{Z}_o$, ***H*** and ***T*** responses. White areas are periods that are not sensitive to the anomalies. Note that all plots have different colour scales. Grey thick lines at the top of each pseudo-section show the location of the studied anomalies along the profile.

greater than one require the presence of 3-D structures (Fig. 7a). The error in β was calculated by computing a thousand β values using different values of the ***Z*** components (Z_{xx}, Z_{xy}, Z_{yx} and Z_{yy}, real and imaginary) randomly distributed within the total range of the assumed error.

For the ***H*** responses dimensionality analysis was performed following similar criteria to that used by Berdichevsky *et al.* (2010b), plotting the variations of the ***H*** responses: ***H-I***, where ***I*** is the identity matrix. In this case 1-D structures are represented by dots (Phi_max = Phi_min = 0), 2-D structures by lines (Phi_max > Phi_min = 0) and 3-D structures by ellipses (Phi_max ≥ Phi_min ≠ 0). The colour represents the magnitude of Phi_min divided by the error of Phi_min. Only values greater than one require the presence of 3-D structures to explain the observed responses (Fig. 7b). Error in Phi_min values were derived following equivalent steps to that the calculation of the error in β.

Finally, induction arrows (Schmucker 1970), following the Parkinson criteria (i.e. the real arrows generally point towards current concentrations in conducting anomalies, Jones 1986), were used to study the dimensionality of the area using the ***T*** responses (Fig. 7c). For the ***T*** responses, the presence of real and imaginary arrows pointing in non-parallel directions at the same period and site is associated with a 3-D structure, as the imaginary induction arrow is approximately parallel to the difference between two real induction arrows at consecutive periods at the same site (Marcuello *et al.* 2005). The coloured circles show the differences between the angle of the real and the imaginary arrows, for each period and site, divided by the error at constraining the angle difference. Note that to define the angle difference between real and imaginary arrows we computed the differences using the same and opposite directions of the real and imaginary arrows, and selected the minimum angle difference value. Values greater than one at dividing the angle difference by the error at determining the angle difference suggest the presence of 3-D structures (Fig. 7c). Errors at defining the angle difference between real and imaginary arrows were derived following equivalent steps to that the calculation of the error in β.

Comparing the results in Fig. 7 between all sites and periods, differences between the angles of the phase tensor ellipses (removing the 90° ambiguity), the directions of the arrows (***T*** responses) and the angles of Phi_max (***H*** responses), all of them are also related to a 3-D environment. Note that for structures crossing the MT profile (L1 and H1), the phase tensor and the induction arrows appear to characterize the 3-D behaviour at the sites located at the edges of the anomalies, whereas looking at the variations of ***H***, sites located

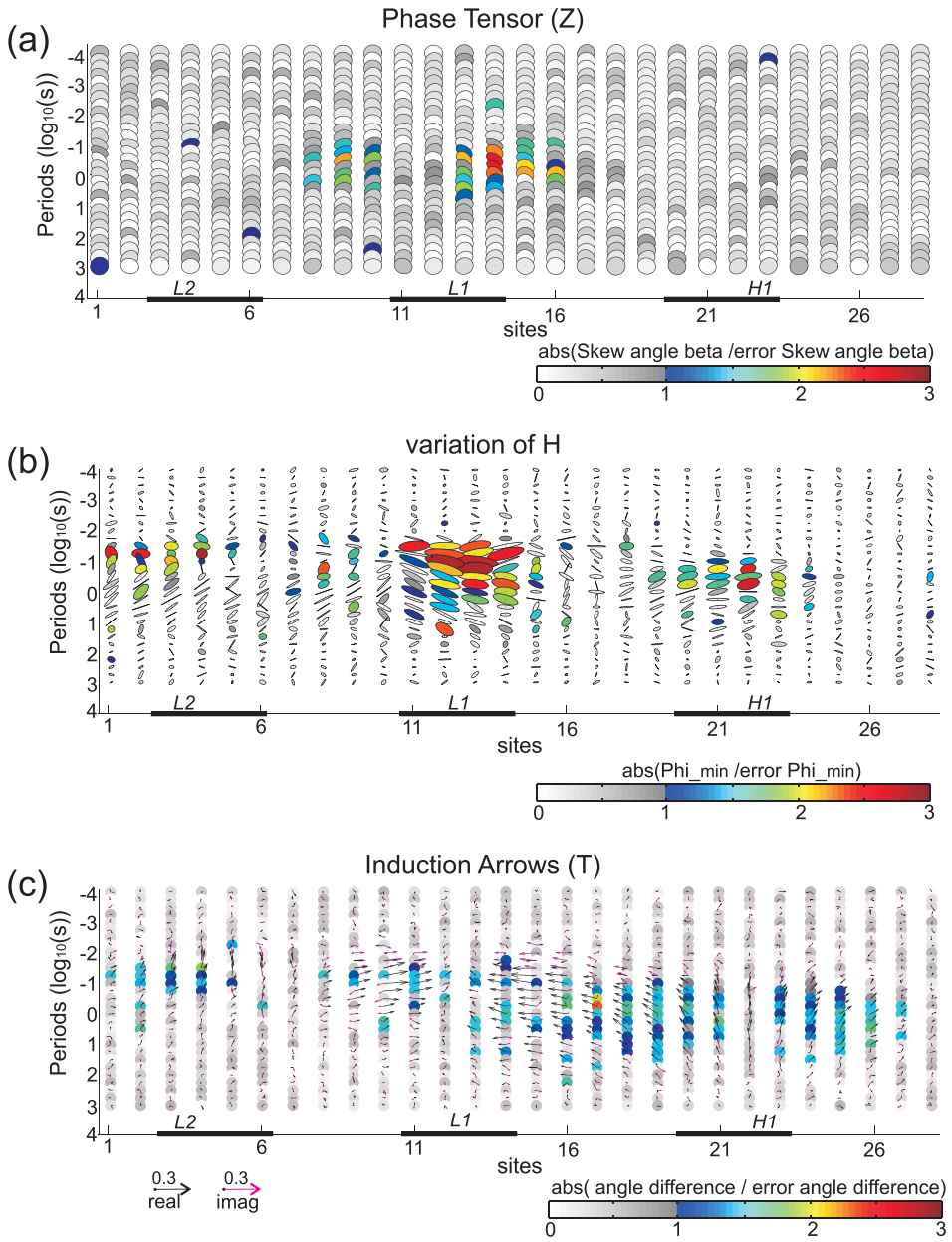

Figure 7. (a) Phase tensor dimensionality analysis using ***Z*** responses. White-grey colours are periods affected by signal associated with 1-D or 2-D structures. Rainbow colours are periods affected by signal associated with 3-D anomalies. (b) Results from the dimensionality analysis using variations of the ***H*** responses (***H***–***I***), where ***I*** is the identity. Dots are related to periods affected by signal associated with 1-D structures. Lines are related to periods affected by signal associated with 2-D structures. Ellipses are related to periods affected by signal associated with 3-D anomalies. White-grey colours are periods that, because of the assumed errors, do not require the presence of 3-D anomalies. Rainbow colours are periods affected by signal that, even with the assumed errors, requires the presence of 3-D anomalies. (c) Induction arrows from ***T*** responses, following the Parkinson criteria, used to characterize the dimensionality of the area. White-grey colours are periods that, because of the assumed errors, do not require the presence of 3-D anomalies. Rainbow colours are periods affected by signal that, even with the assumed errors, requires the presence of 3-D anomalies.

above of the anomalies seems to be more affected by the 3-D effect of the anomalies.

2.5 3-D inversion of the MT profile

Nine inversions were performed using different combinations of ***Z***, $\boldsymbol{Z}_o$, ***H*** and ***T*** responses employing the ModEM algorithm (Egbert & Kelbert 2012; Kelbert *et al.* 2014) modified for inclusion on ***H*** responses (see Fig. S1, for more details). In all cases, the same inversion parameters were used to avoid differences associated with inversion set-up parameters and thus focusing only on the differences related to the investigated data types.

2.5.1 Inversion parameters

The 3-D solution mesh, purposely chosen with a lower resolution than the forward mesh described above, comprised 137 × 120 × 99 cells in the north–south, east–west and vertical directions, respectively. The centre of the mesh comprised 99 × 62 × 99 cells with a horizontal cell size of 200 m × 200 m, while the distance

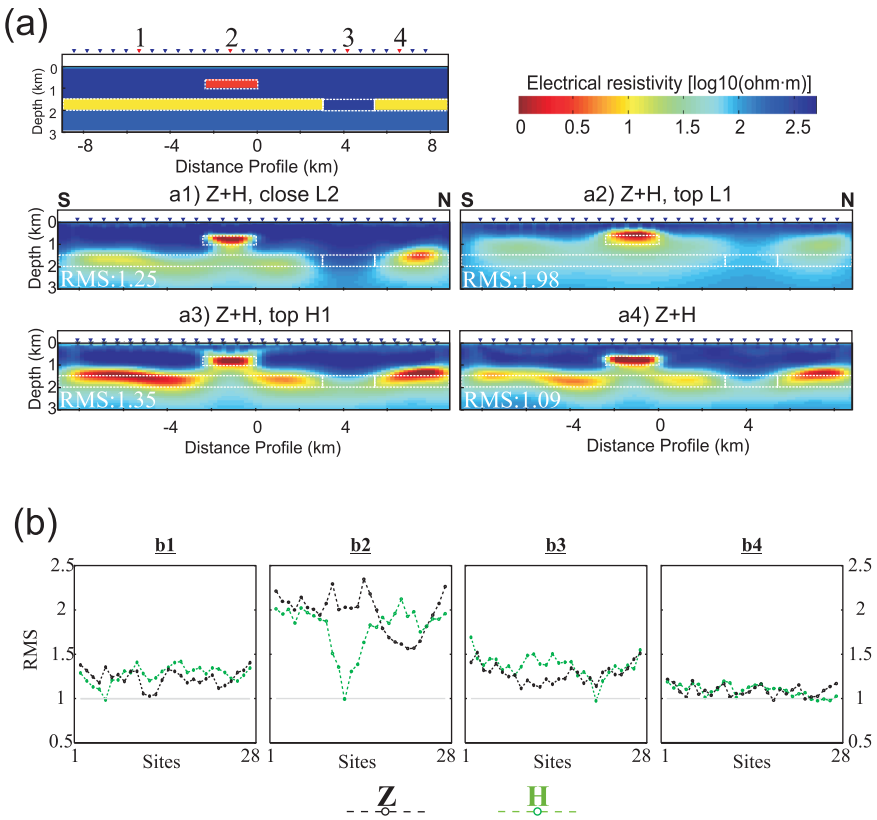

Figure 8. (a) Results of the different inversion process below the MT profile using neighbouring reference sites located at different places along the MT profile. White dashed lines are plotted to better compare the results with the original synthetic model. (b) nRMS of each inversion processes for each site and for each type of data. Circles are the nRMS of the corresponding site.

between sites was 600 m, thus ensuring the presence of free cells between the sites. The lateral extent of the padding cells increased by a factor of 1.3. The thickness of the top layer was 10 m, increasing by a factor of 1.069 for the subsequent layers in the z-direction. The same responses studied in the dimensionality analysis, with added noise, were used for the inversion process, but only for periods between 0.0001s (frequency of 10 000 Hz) and 31.62 s (frequency of 0.0316 Hz), focusing on the periods affected by the anomalies and avoiding the periods affected by the assumed hypothetical asthenosphere at 90 km depth.

Several tests were executed to choose the initial electrical resistivity model and the smoothing parameters. The starting model was chosen after inverting the $\boldsymbol{Z}$ responses, which are sensitive to lateral–vertical variations and to the actual resistivity of the subsurface, with seven different half-space starting models of 80, 100, 120, 150, 200 and 400 Ωm, respectively. Inversion results starting with a half-space model of 120 Ωm recovered the most similar electrical resistivity values to the synthetic model used to generate the synthetic data, having a lower average distance between the final inversion result and the original synthetic model. For all the inversions a similar normalized root mean square (nRMS) was obtained regardless of the different starting models. The smoothing values used for this test were 0.3 in all directions. As shown below, these smoothing values do not differ significantly from the smoothing values finally used during the inversion problem.

It is well known that regularization, necessary in any ill-posed inverse problem, has a large influence on the results of the inversion and particularly on resolution. In the case of the ModEM code we have to choose horizontal and vertical smoothing parameters. To take care of that, we performed additional tests to determine the appropriate regularization parameters, being aware that different data types may react differently to the same smoothing parameters. Inverting $\boldsymbol{Z}$ and $\boldsymbol{Z} + \boldsymbol{T} + \boldsymbol{H}$ several combinations of horizontal and vertical smoothing parameters were executed using smoothing values between 0.1 and 0.6 (always assuming the same smoothing values for north–south and east–west directions). Searching for the simplest model that can fit the data, the largest smoothing parameters were chosen that adequately recover the synthetic model while still allowing the inversion processes to fit the data within the error bars. Based on these tests, the chosen starting model for all the inversions presented in this manuscript was a homogeneous half-space of 120 Ωm, and the smoothing values for all the inversions were 0.4 for north–south and east–west directions, and 0.3 for the vertical direction. Note that despite a smoothing of 0.5 for the north–south and east–west direction was also appropriate to fit $\boldsymbol{Z}$ data, it was not appropriate when inverting the combined $\boldsymbol{Z} + \boldsymbol{T} + \boldsymbol{H}$ responses, suggesting that the joint inversion process including all possible data requires more detail in the model to fit the data. No outstanding differences were observed when using 0.5 or 0.4 smoothing parameter for north–south and east–west directions when performing the inversion process with $\boldsymbol{Z}$ data. In the presented inversions, the a priori model was the same as the initial model (both are homogeneous), assuming that there is no prior information about the electrical resistivity values of the subsurface.

An additional test was performed to evaluate if the choose neighbouring reference site for the $\boldsymbol{H}$ responses in the sensitivity test was adequate for the inversion process. Four inversions with $\boldsymbol{Z}$ and $\boldsymbol{H}$ responses were performed using four different reference sites for

the $\boldsymbol{H}$ responses: (1) using a site close to the L2 anomaly; (2) on top of the L1 anomaly; (3) on top of the H1 anomaly; (4) as in the sensitivity test, on top of a non-complex environment (almost 1-D). Results from the inversion process (Fig. 8a) show that locating the reference site on top of a non-complex environment, such as the one used for the sensitivity test, facilitate convergence of the inversion process (lower nRMS) also obtaining the model that better recovers the original synthetic model. Fig. 8(b) shows the nRMS of each inversion for each site and data type. From the results of this test, it is strongly recommended not to use a reference site on top of anomalies (L1 and H1 in our case), in particular on top of a strong conductive anomaly such as L1. In this experiment, the inversion process using a reference site on top of L1 was not able to fit the data and the obtained model was the one that recovered the original synthetic model worst of all (Fig. 8). The inversion process using a neighbouring reference site close to L2 also does not converge to an nRMS lower than 1.2 but the model from the inversion process is superior to the two cases where the neighbouring reference site was on top of L1 and H1 anomalies. Note that the nRMS for the $\boldsymbol{H}$ response associated with the neighbouring reference site is always close to 1 in all cases. This is because the $\boldsymbol{H}$ responses compare the signal between two sites, and the signal between the neighbouring site with itself is the same. The fact that it is one and not zero is because of the noise we added in the responses. For the following inversions presented in this manuscript, the same site as the one used in the sensitivity test was used as a reference site for the $\boldsymbol{H}$ responses.

For the numerical experiment, four inversions were performed to examine and highlight the improvements that can be made by complementing the $\boldsymbol{Z}_o$ and $\boldsymbol{Z}$ responses with the $\boldsymbol{T}$ and $\boldsymbol{H}$ responses, whilst also evaluating the necessity of using diagonal components of $\boldsymbol{Z}$ in these situations. The final inversions were (1) $\boldsymbol{Z}_o$, (2) $\boldsymbol{Z}$, (3) $\boldsymbol{Z}_o + \boldsymbol{H} + \boldsymbol{T}$ and (4) $\boldsymbol{Z} + \boldsymbol{H} + \boldsymbol{T}$. Four additional inversions, (5) $\boldsymbol{Z}_o + \boldsymbol{H}$, (6) $\boldsymbol{Z}_o + \boldsymbol{T}$, (7) $\boldsymbol{Z} + \boldsymbol{H}$ and (8) $\boldsymbol{Z} + \boldsymbol{T}$ were performed to differentiate the contributions of the $\boldsymbol{H}$ and $\boldsymbol{T}$ responses independently. Finally, the capacity of the $\boldsymbol{H}$ and $\boldsymbol{T}$ responses to characterize the subsurface by themselves was considered in inversion (9) $\boldsymbol{H} + \boldsymbol{T}$. This latter one is interesting as no electric fields are involved, thus there should be primary sensitivity to lateral conductivity variations rather than to the absolute values of the conductivities themselves.

2.5.2 Results

The results are displayed showing a north–south section of the obtained electrical resistivity models beneath the MT profile and with horizontal slices of the models at 650 and 1550 m depths. Fig. 9 shows the results of inversion (1) $\boldsymbol{Z}_o$, (2) $\boldsymbol{Z}$, (3) $\boldsymbol{Z}_o + \boldsymbol{H} + \boldsymbol{T}$ and (4) $\boldsymbol{Z} + \boldsymbol{H} + \boldsymbol{T}$, highlighting the advantages of complementing $\boldsymbol{Z}$ or $\boldsymbol{Z}_o$ with $\boldsymbol{H}$ and $\boldsymbol{T}$. Fig. 10 displays the results of inversions (5) $\boldsymbol{Z}_o + \boldsymbol{T}$, (6) $\boldsymbol{Z}_o + \boldsymbol{H}$, (7) $\boldsymbol{Z} + \boldsymbol{T}$, (8) $\boldsymbol{Z} + \boldsymbol{H}$ and (9) $\boldsymbol{H} + \boldsymbol{T}$ demonstrating the consequences of different contributions of $\boldsymbol{H}$ and $\boldsymbol{T}$ responses. The same colour scale was used in all figures. White dashed lines indicate the positions of the main resistivity structures, L1, L2, L3 and H1, to facilitate the comparison of the obtained inversion results with the original synthetic model.

2.5.2.1 Fit of the data. The fit of the data of each inversion process is shown in Fig. 11 plotting the summed nRMS as calculated in the ModEM code (Egbert & Kelbert 2012; Kelbert *et al.* 2014) for each site, type of response and for each type of inversion, providing valuable information on how data misfit distributes along the profile for different inversions and different response types. Different colours were used for each type of response: red for $\boldsymbol{Z}_o$ responses, black for $\boldsymbol{Z}$ responses, blue for $\boldsymbol{T}$ responses, and green for $\boldsymbol{H}$ responses. No systematic problems related to overfitting were observed with a particular response type or site locations, although some of the sites positioned at the edges of the profile have slightly larger nRMS than the ones located within the profile. Note that the nRMSes associated with $\boldsymbol{Z}$ and $\boldsymbol{Z}_o$ responses are similar when only $\boldsymbol{Z}$ or $\boldsymbol{Z}_o$ were used in the inversion process or when they were combined with $\boldsymbol{T}$ and $\boldsymbol{H}$ responses during the inversion process. This result shows that all datasets are fit to a similar level and that no remarkable decrease in resolution of a particular type of response is observed when other responses are used during the inversion process.

More detailed information about the fit of the data can be found in Fig. S2, where differences between data and model responses divided by the error were plotted for each type of inversion, component of the data, site and period in a pseudo-section format. Grey areas are periods with differences lower than the error; red and blue areas are periods with differences larger than the errors.

2.5.2.2 Electrical resistivity model beneath the MT profile. Models resulting from inversion of the $\boldsymbol{Z}_o$ or $\boldsymbol{Z}$ responses (Figs 9a1 and a2) show the existence and presence of the main anomalies but do not resolve or characterize them well; in particular the resistivity values directly below L1 are poorly resolved due to the shielding effects of L1. These two models appear to be unable to differentiate between anomaly L1 and the conducting anomalous layer L3 that underlies L1, implying a continuous horst-like structure with the L3 getting shallow to the depths of L1 in the middle of the profile. Additionally, the high electrical resistivity anomaly H1 is inferred but not well recovered, showing resistivity values around 80 Ωm, which are almost an order of magnitude lower than the correct value (400 Ωm). Note that these values (∼80 Ωm) are also lower than the initial half-space model used for the inversion process (120 Ωm). The use of the $\boldsymbol{H}$ and $\boldsymbol{T}$ responses as complements to the $\boldsymbol{Z}_o$ or $\boldsymbol{Z}$ responses (Figs 9a3 and a4) significantly improves resolution of all targets, conductive and resistive, showing L1 and L3 structures as disconnected ($\boldsymbol{Z} + \boldsymbol{H} + \boldsymbol{T}$) or almost disconnected ($\boldsymbol{Z}_o + \boldsymbol{H} + \boldsymbol{T}$), thus better constraining the bottom of anomaly L1 and clearly recovering anomaly H1 in the northern part of the profile. The use of the $\boldsymbol{H}$ and $\boldsymbol{T}$ responses also better defines the north and south boundaries of anomalies L1 and H1. By complementing the $\boldsymbol{Z}_o$ or $\boldsymbol{Z}$ responses with $\boldsymbol{T}$ and $\boldsymbol{H}$ responses, the continuity of the low resistivity layer (L3) is better defined, although in none of the models is the continuity of L3 correctly recovered below L1 due to the electromagnetic shielding effects of L1 to any structure immediately below it.

2.5.2.3 Horizontal slices at 650 and 1550 m depth. The horizontal slices through the various 3-D resistivity models at 650 m depth are shown in Fig. 9(b). If only the $\boldsymbol{Z}_o$ responses are inverted, the model is symmetrical on both sides of the profile, thus characterizing the anomalies to extend outside of the profile but without indicating on which side the anomalies are located. This illustrates and emphasizes that the off-diagonal components contain no directional information for off-profile structures. The use of diagonal components in inversion of the full $\boldsymbol{Z}$ responses characterizes the dimensionality of the structures whilst locating L2 to be west of the MT profile and inferring the westerly extension of L1 (compare Fig. 9b1 with Fig. 9b2). From Figs 9(b3) and (b4) it is clear that by complementing the $\boldsymbol{Z}_o$ or $\boldsymbol{Z}$ responses with $\boldsymbol{H}$ and $\boldsymbol{T}$ responses the correct dimensionality of the structures is recovered in both cases, showing in particular a remarkable improvement when $\boldsymbol{Z}_o$ responses

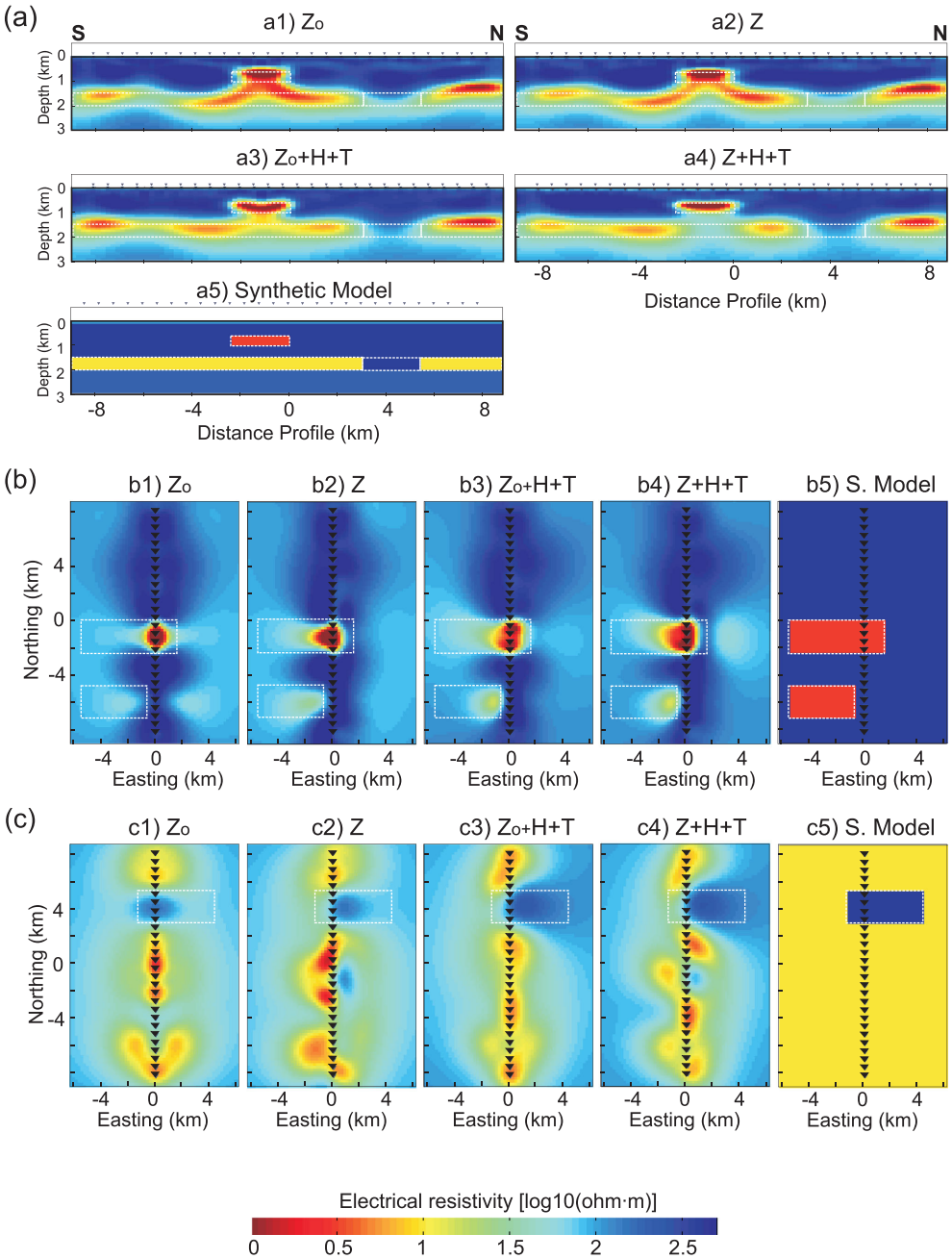

Figure 9. (a) Results of the different inversion process below the MT profile. (b) Horizontal slices showing the results of the inversion processes at 650 m depth. (c) Horizontal slices showing the results of the inversion processes at 1550 m depth. (a5), (b5) and (c5) are the original synthetic model. White dashed lines are plotted to better compare the results with the original synthetic model.

are complemented with $\boldsymbol{H}$ and $\boldsymbol{T}$ responses. Fairly equivalent models are obtained from the $\boldsymbol{Z}_o + \boldsymbol{H} + \boldsymbol{T}$ and $\boldsymbol{Z} + \boldsymbol{H} + \boldsymbol{T}$ responses, but with slightly improved resolution, closer to the original synthetic model, when using $\boldsymbol{Z} + \boldsymbol{H} + \boldsymbol{T}$. The use of the $\boldsymbol{H}$ and $\boldsymbol{T}$ responses also improves the characterization of L2 by showing more reliable low resistivity values than when only using $\boldsymbol{Z}_o$ or $\boldsymbol{Z}$ responses, even if the resistivity values are still higher than in the original synthetic model. Additionally, the north and south boundaries and the east and west propagation of L1 are better defined when complementing the $\boldsymbol{Z}_o$ or $\boldsymbol{Z}$ responses with the $\boldsymbol{H}$ and $\boldsymbol{T}$ ones.

Fig. 9(c) shows the horizontal slices of the final 3-D models at 1550 m depth. At this depth the synthetic model is a uniform 10 Ωm conducting layer (defined as anomaly L3) within which a 400 Ωm resistive anomaly (H1) is embedded. Models from the conventional MT, $\boldsymbol{Z}_o$ and $\boldsymbol{Z}$, responses (Figs 9c1 and c2), exhibit a more complex situation than might be expected from the original synthetic model, somewhat suggesting the presence of the H1 anomaly with the highest electrical resistivity values (∼100 Ωm) either directly below or outside of the profile, which is still lower than the 120 Ωm of the starting model used for the inversion process. By carrying out joint inversion including the $\boldsymbol{H}$ and $\boldsymbol{T}$ responses, the models better define the L3 layer and more accurately recover H1 below and outside the MT profile, with electrical resistivity values of around 250 Ωm, which is greater than the 120 Ωm of the starting model used for the inversion process (Figs 9c3 and c4) and closer to the 400 Ωm of the original synthetic model (Fig. 9c5).

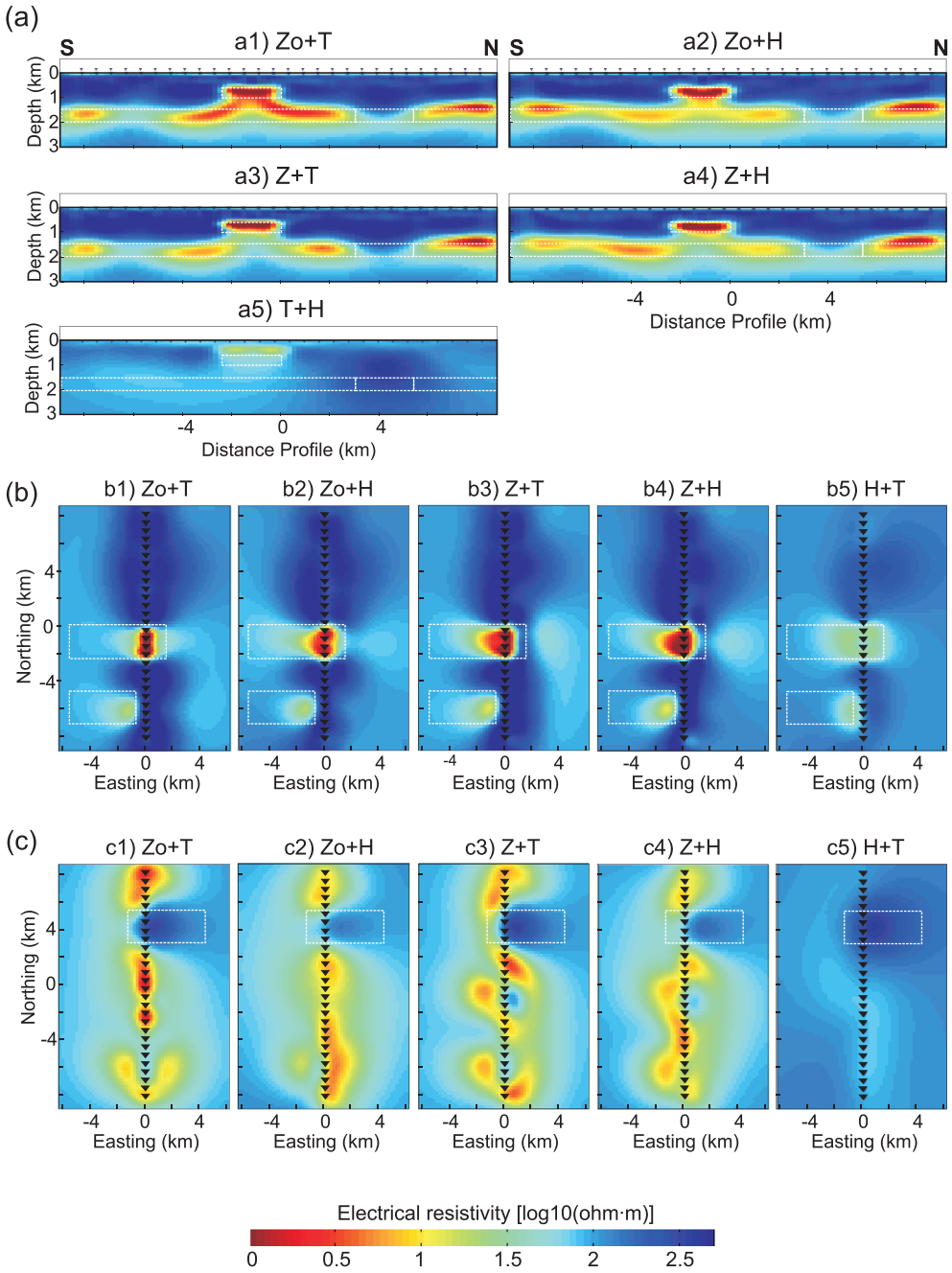

Figure 10. (a) Results of the different inversion processes beneath the MT profile. (b) Horizontal slices showing the results of the inversion processes at 650 m depth. (c) Horizontal slices showing the results of the inversion processes at 1550 m depth. White dashed lines are plotted to better compare the results with the original synthetic model.

2.5.2.4 Contribution of ***H*** *and* ***T****.* Fig. 10 shows the results of the inversion process combining $\boldsymbol{Z}_o$ and $\boldsymbol{Z}$ responses with either $\boldsymbol{T}$ or $\boldsymbol{H}$ responses separately. From Fig. 10(a), results below the profile, it can be seen that the inclusion of the $\boldsymbol{H}$ responses is responsible for superior differentiation between L1 and L3. This differentiation also occurs when inverting $\boldsymbol{Z} + \boldsymbol{T}$ but not when $\boldsymbol{Z}_o$ is complemented with $\boldsymbol{T}$ responses ($\boldsymbol{Zo} + \boldsymbol{T}$), that is the use of diagonal terms of the impedance tensor is key to resolving the lack of interconnection between L1 and L3. In addition, the $\boldsymbol{H}$ responses contribute to better defining the continuity of the low electrical resistivity L3 layer. The main improvement gained by using the $\boldsymbol{T}$ responses is superior definition of the north and south boundaries of L1.

Fig. 10(b) shows the results at 650 m depth when inverting the $\boldsymbol{H}$ or $\boldsymbol{T}$ responses as a complement to the $\boldsymbol{Z}_o$ and $\boldsymbol{Z}$ responses. In all cases, comparing with the results in Figs 9(b1) and (b2), the resolution and characterization of the anomalies are improved, especially in defining the L2 anomaly. The main differences between complementing with either the $\boldsymbol{H}$ or $\boldsymbol{T}$ responses are observed when characterizing the propagation of anomaly L1 to the west, which is constrained by the $\boldsymbol{H}$ and $\boldsymbol{Z}$ responses but not by the $\boldsymbol{T}$ responses, as expected from our sensitivity tests above. Fig. 10(c) displays the model slices at 1550 m depth, showing the contribution of including the $\boldsymbol{H}$ and $\boldsymbol{T}$ responses separately from each other (*cf.* Fig. 9c). In all cases, the use of either or both the $\boldsymbol{H}$ and $\boldsymbol{T}$ responses lead to superior

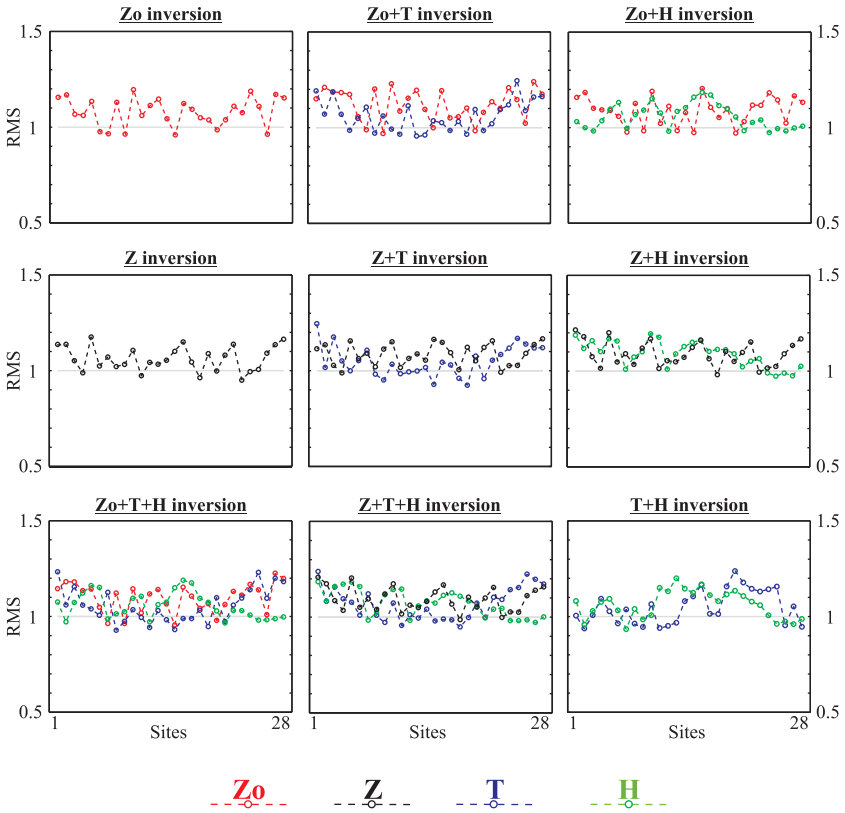

Figure 11. nRMS of each inversion processes for each site and for each type of data. Circles are the nRMS of the corresponding site. Excellent nRMS misfits of between 1.0 and 1.1 were achieved for all inversions using different types of responses.

recovery of the H1 anomaly and show its propagation to the east. Fig. 10(c) also shows that by using the ***H*** responses as a complement to the ***Z*** and $\boldsymbol{Z}_o$ responses, the models better reproduce the electrical resistivity values of the original synthetic model off-profile.

Figs 10(a5), (b5) and (c5) show that the magnetic-field only ***H*** and ***T*** responses alone are insufficient to characterize the subsurface by themselves. The associated models locate the anomalies along the north–south and east–west directions, but have no resolution in the vertical direction and do not recover the electrical resistivity values. This is because the magnetic field is sensitive to lateral resistivity contrasts (both amplitude and position), but is insensitive to 1-D layering and to the actual resistivity values of the synthetic model.

2.5.2.5 Accuracy of the models. One way to quantify how well the models obtained from the inversion process reproduce the synthetic model is to calculate the differences between them in model space. We have calculated these differences with a focus on the structures below the profile, where we expect to obtain higher resolution. Fig. 12 shows the differences between the synthetic model and the models obtained from the inversion process, using decadic logarithm electrical resistivity values. Blue colours indicate results from the inversion process that are more resistive than the synthetic model, red colours indicate results more conductive than the synthetic model, and white colours indicate an almost-perfect fit between the inversion process model and the synthetic model. Note that the colour scale indicates differences between the two models that are greater than ± 0.023; this value is equivalent to a difference of approximately ± 0.5 Ωm for electrical resistivity values of 10 Ωm, and a difference of approximately ± 50 Ωm for electrical resistivity values of 1000 Ωm. The average differences for each type of inversion are shown in Table 1.

These results indicate the superior performance when reproducing the electrical resistivity values of the synthetic model when the ***Z*** or $\boldsymbol{Z}_o$ responses are combined with ***T*** and ***H*** responses. The results also corroborate that the electrical resistivity values obtained when using only the ***T*** and ***H*** responses are not correctly reproduced.

By conducting a more detailed analysis of Fig. 12, the following important points associated with the recovering of each anomaly become apparent:

(1) *Structure L1*: The edges and bottom are better recovered when ***T*** and ***H*** responses are each or both involved in the inversion process. Despite the electrical resistivity values always remaining more conductive than in the synthetic true model, they are better recovered when the ***H*** responses are included in the inversion process.

(2) *Structure H1*: In all the inversion processes the electrical resistivity values associated with H1 are less resistive than in the synthetic model, however, recovery of these resistivity values, and the geometry of the anomaly, is always improved when the ***H*** and ***T*** responses are each or both involved in the inversion process.

(3) *Structure L3*: The electrical resistivity values are improved when the ***H*** responses are included in the inversion process. Note that when the ***T*** responses are used in the inversion process, the top of the anomaly is also better characterized, particularly in the southern part of the profile.

(4) *Background 1-D model*: Results from the inversion processes complementing ***Z*** or ***Z***o with the ***H*** responses are the ones that best recover the electrical resistivity values of the background 1-D

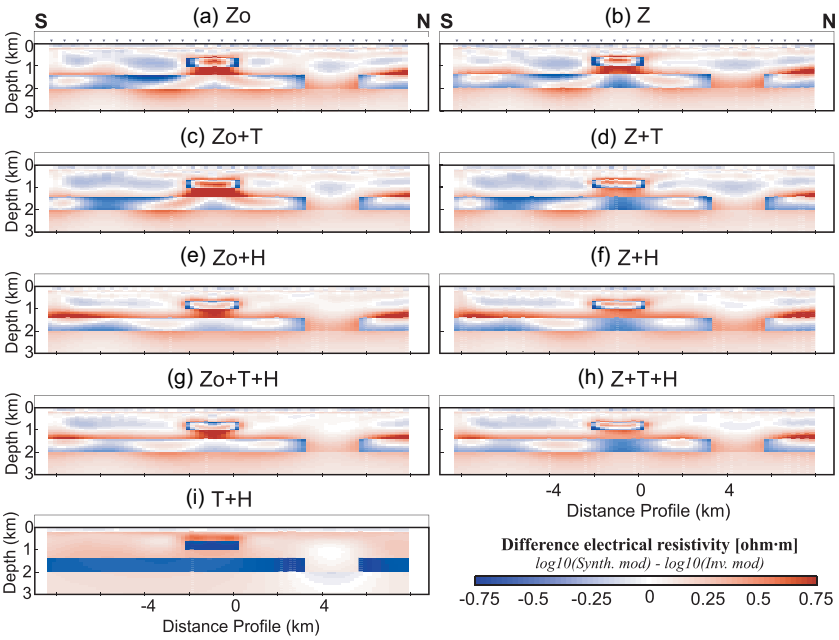

Figure 12. Differences, using decadic logarithm electrical resistivity values, between models obtained from the inversion process and the synthetic model.

Table 1. Average differences between the final inversion models and the original synthetic model. Differences calculated using log10 electrical resistivity values.

Inverted data	$\boldsymbol{Z}_o$	$\boldsymbol{Z}$	$\boldsymbol{Z}_o + \boldsymbol{H} + \boldsymbol{T}$	$\boldsymbol{Z} + \boldsymbol{H} + \boldsymbol{T}$	$\boldsymbol{Z}_o + \boldsymbol{T}$	$\boldsymbol{Z}_o + \boldsymbol{H}$	$\boldsymbol{Z} + \boldsymbol{T}$	$\boldsymbol{Z} + \boldsymbol{H}$	$\boldsymbol{H} + \boldsymbol{T}$
Difference	0.151	0.149	0.133	0.134	0.144	0.141	0.134	0.138	0.214

resistivity model; not only do the results show smaller differences with respect to the original synthetic model, but they also show a more homogeneous (less blobby) resistivity model than the other inversion results.

3 DISCUSSION

Focusing on the recovery of electrical resistivity structures in 3-D areas, the use of the full impedance tensor responses ($\boldsymbol{Z}$), instead of using only the off-diagonal elements ($\boldsymbol{Z}_o$), is highly recommended for all 3-D inversions because of the far superior capacity to reproduce the dimensionality of the geoelectrical structures in the subsurface. It reaffirms and further validates the conclusions drawn and emphasized previously by Siripunvaraporn *et al.* (2005b), Tietze & Ritter (2013) and Kiyan *et al.* (2014). However, it is not always possible to use all of the components of the MT impedance tensor because diagonal components, being of lower amplitude, are far more affected by the presence of noise. This requires the necessity of including robust complementary information in these situations. Siripunvaraporn & Egbert (2009) highlighted the advantages of using $\boldsymbol{Z} + \boldsymbol{T}$ data during the 3-D inversion process, suggesting that resistivity values, geometry of the anomalies, and depths are all better characterized. However, not all of the studies show major advantages when performing joint inversion of $\boldsymbol{Z} + \boldsymbol{T}$ responses in a 3-D environment. Tietze & Ritter (2013) present a situation where results from $\boldsymbol{Z}$ responses alone are more reliable than the results from $\boldsymbol{Z} + \boldsymbol{T}$ responses. In previous synthetic studies working with $\boldsymbol{T}$ and $\boldsymbol{H}$ responses, Habibian & Oskooi (2014) show that inversion processes using either or both $\boldsymbol{T}$ and $\boldsymbol{H}$ responses have vertical resolution and are able to recover the correct electrical resistivity values of the subsurface, which does not happen in the experiment shown in this manuscript (Fig. 10). However, in the previous study the background structure was homogeneous with uniform resistivity and the same as the one used for the starting model for the inversion. This configuration masks the incapacity of the $\boldsymbol{H}$ and $\boldsymbol{T}$ responses on their own to recover vertical anomalies or the correct electrical resistivity values. The numerical experiment design in this manuscript, using a 1-D layered model as a background, highlight this deficiency of the $\boldsymbol{H}$ and $\boldsymbol{T}$ responses, showing that vertical resolution or the obtained electrical resistivity values from an inversion using either or both $\boldsymbol{T}$ and $\boldsymbol{H}$ responses are only reliable if additional information defining the background structures of the study area is added. However, complementing $\boldsymbol{Z}$ and $\boldsymbol{Z}_o$ responses, $\boldsymbol{T}$ and $\boldsymbol{H}$ aids superior determination of the electrical resistivity values of the subsurface, including the characterization of the absolute electrical resistivity values (see Table 1 and Fig. 12). Results from Varentsov (2015a,b) combining $\boldsymbol{Z}$, $\boldsymbol{H}$ and $\boldsymbol{T}$ responses using 2-D, 2-D + and a quasi 3-D approaches encourage the use of $\boldsymbol{H}$ responses for the inversion process, improving the accuracy of the results, and better separating close spaced conductors in complex geoelectrical situations.

In this work, the advantages of using $\boldsymbol{T}$ and $\boldsymbol{H}$ responses as a complement to $\boldsymbol{Z}$ or $\boldsymbol{Z}_o$ responses in a 3-D environment are evaluated from the results of a numerical experiment. Starting with the sensitivity of each response type to the studied anomalies, the results of our numerical experiment exhibit that both the $\boldsymbol{H}$ and $\boldsymbol{T}$ responses are also sensitive to the dimensionality of the structures and can be used to successfully reproduce the dimensionality of the anomalies when complementing $\boldsymbol{Z}_o$ or $\boldsymbol{Z}$ responses (Figs 9 and 10). The sensitivity tests performed (Fig. 6) demonstrate that the $\boldsymbol{Z}_o$ and

Z responses are intrinsically more sensitive to the existence of the anomalies than are the ***H*** and ***T*** responses. However, the dimensionality analysis (Fig. 7) and the capacity for recovering the detail of the geoelectrical structures (Figs 9, 10 and 12) are remarkably improved when the $\boldsymbol{Z}_o$ or ***Z*** responses are complemented with either, and especially both, the ***H*** and ***T*** responses. Each response type has a specific behaviour when characterizing the dimensionality of the structures and consistency between all of them will support the ultimately adopted dimensionality of the study area. The use of the ***T*** and ***H*** responses can also improve the dimensionality analysis in situations where the phase tensor is not a strong tool; see for example the results close to the L2 and H1 anomalies (Fig. 7). In that case the phase tensors do not correctly define the presence of 3-D structures having no periods showing absolute values of the β angle divided by the associated error greater than 1. However, by using the ***H*** and ***T*** responses the characterization of 3-D structures of these areas is significantly improved. Comparing the dimensionality analysis from the ***H*** and ***T*** responses close to resistive anomaly H1, induction arrows clearly point in different directions than the direction of Phi_max from the ***H*** responses, which is also suggestive of a 3-D situation.

Focusing now on the ability of recovering the correct electrical resistivity distribution of the subsurface, the observed improvements are associated with the use of different types of responses that better restrict the model space than if any are used individually. More specifically, this phenomenon occurs because the ***Z*** responses are far more sensitive to the L1 anomaly than to the L2 and H1 anomalies, whereas for our model the ***T*** and ***H*** responses have similar sensitivity to all of the anomalies (Fig. 6). Such sensitivity means that the inversion of the $\boldsymbol{Z}_o$ or ***Z*** responses focuses mainly on L1, with less importance placed upon the L2 and H1 anomalies. Results from the sensitivity tests (Figs 2–5) can also be used to understand how inclusion of the ***H*** and ***T*** responses improves the characterization of the subsurface.

Inspecting the resolved structures beneath the MT profile (Figs 9, 10 and 12), four main improvements are apparent when performing joint inversion of the $\boldsymbol{Z}_o$ or ***Z*** responses with ***H*** and ***T*** ones:

(1) Characterization of the bottom of the L1 anomaly with better differentiation between the L1 and L3 structures;
(2) The possibility of recovering the high resistivity anomaly, H1, surrounded by low resistivity values, L3, that are poorly recovered when using only $\boldsymbol{Z}_o$ or ***Z*** responses;
(3) Better resolution in determining the resistivity values of the subsurface, obtaining results more similar to the original synthetic model;
(4) Superior definition of the shape of the anomalies in the north–south direction, i.e. along profile, with a better fit inside the white dashed lines in the figures.

Despite all these advantages, we would like to point out that in all models the location of the L3 layer at the edges of the profile is somewhat shallower than what it should be. This problem is not properly corrected when complementing ***Z*** or ***Zo*** with ***T*** and ***H*** responses, although results with ***T*** responses seem to slightly improve the depth of the conductive layer L3 (Figs 9, 10 and 12).

Looking outside the line of the profile (Figs 9b, c and 10b, c), L2 and H1 are better recovered when the inversion is complemented with ***H*** and ***T*** responses. However, although the characterization of the off-profile anomalies is improved when complementing the ***Z*** responses with the ***H*** and ***T*** ones, the shape of the anomalies and the electrical resistivity values are still not properly constrained, probably as a consequence of a combination of (i) the non-uniqueness of the MT method, and (ii) scatter and error.

Inspecting the results obtained from the ***T*** responses, the main signal associated with the anomalies is located at the edge of the structures (Figs 2–6), making the ***T*** responses a good type of data to define boundaries of the structures along the MT profile. Note that from Fig. 6(d) this edge-detection is more precise for low resistivity anomalies (L1) than for high resistivity anomalies (H1). This can also be observed when recovering the anomalies from the inversion process (Figs 9 and 10) where the north and south boundaries of L1 and H1 are improved when the ***T*** responses are included. This result, highlighting the capacity of the ***T*** responses characterizing the edges of the anomalies, is consistent with previous results, such as Siripunvaraporn & Egbert (2009) and Habibian & Oskooi (2014). In addition, the top of the low electrical resistivity layer L3 is improved when the inversion of ***Z*** or $\boldsymbol{Z}_o$ data is complemented with ***T*** data (Figs 10a1, a3, 12c and d). This makes ***T*** data a good complement to improve the definition in recovering the edges and shape of the anomalies below a profile located in a 3-D environment, in agreement with results suggested by Siripunvaraporn & Egbert (2009). Note that, apart from the H1 anomaly, no major improvement associated with the use of ***T*** responses has been observed in defining the electrical resistivity values of the anomalies or the background 1-D model (Figs 12c and d). Results from Fig. 10 shows that, although the use of ***T*** data as a complement of $\boldsymbol{Z}_o$ provides an improvement in characterizing the subsurface, the results are remarkably better when ***Z*** and ***T*** responses are both used in the inversion process.

Examining the results from the ***H*** responses, the major advantage is that their use makes the resistivity model more consistent as a whole as all the sites are related to the neighbouring reference site and the intensity of the anomalies tend to be consistent along the whole profile. This effect is also observed in the sensitivity test (Figs 4b and 6c). In this case the neighbouring reference site is located close to H1 and is affected by its presence, which is why the effect of H1 can be seen at sites south of the profile. This property of ***H*** responses increases the consistency of the model as a whole for shallow and deep structures independently of the extension of the area of the study. This level of consistency is not required when using the $\boldsymbol{Z}_o$, ***Z*** or ***T*** responses, where each site is mostly focused on the anomalies nearby but without any explicit link to anomalies that are located far away along the study area, where the periods of the site are insensitive. The consequences of this property in the inversion process can be seen in Fig. 12, where the models including the ***H*** responses obtain electrical resistivity values of the anomalies and the background 1-D resistivity model closer to the original synthetic model. Note that from Fig. 10, although results are better quality when $\boldsymbol{Z} + \boldsymbol{H}$ are used in the inversion process, instead of $\boldsymbol{Z}_o + \boldsymbol{H}$, differences are not as remarkable as the differences observed between $\boldsymbol{Z} + \boldsymbol{T}$ and $\boldsymbol{Z}_o + \boldsymbol{T}$, having similar results from both types of inversion. Note also that, from the performed test shown in Fig. 8, to facilitate and improve the results from the inversion process using ***H*** responses it is recommended to use a neighbouring reference site located on top of a non-complex geoelectrical area. Results from the dimensionality analysis or from prior inversions using ***Z*** alone or $\boldsymbol{Z} + \boldsymbol{T}$ can be used to choose the optimum neighbouring reference site for $\boldsymbol{Z} + \boldsymbol{H}$ or $\boldsymbol{Z} + \boldsymbol{T} + \boldsymbol{H}$ inversion.

4 CONCLUSIONS

The use of the ***H*** and ***T*** responses is demonstrated to be a crucial complement to the $\boldsymbol{Z}_o$ or ***Z*** ones in order to better resolve and

characterize the structures beneath MT profiles in 3-D environments. For the synthetic model considered here, large differences were seen whether the diagonal components of $\boldsymbol{Z}$ were used or not, having far better results when the diagonal components were included. These differences were reduced when including the $\boldsymbol{H}$ and $\boldsymbol{T}$ responses in the inversion process, although results using the diagonal components of $\boldsymbol{Z}$ still recover the subsurface better than when the diagonal components are not used. From the results of this experiment, four main improvements are observed when carrying out joint inversion of the $\boldsymbol{Z}_o$ or $\boldsymbol{Z}$ responses with the $\boldsymbol{H}$ and $\boldsymbol{T}$ ones:

(1) More accurate characterization of the electrical resistivity values of the studied anomalies and also of the background resistivity model;

(2) Superior capability for recovering high electrical resistivity anomalies than by using the $\boldsymbol{Z}_o$ or $\boldsymbol{Z}$ responses alone;

(3) Improved definition of the bottom of low electrical resistivity anomalies and the north, south, east and west boundaries of the anomalies beneath and outside the MT profile; and

(4) Superior imaging of the horizontal continuity of low electrical resistivity anomalies.

Additionally, note that the use of the $\boldsymbol{H}$ responses increases the reliability of the resistivity model as a whole, reducing the possibility for the inverse problem to generate spurious anomalies if the anomaly is not consistent with the data acquired at the neighbouring reference site. Although any site could be used as a neighbouring reference site, as far as the structures below the neighbouring reference site are properly constrained, it is recommended to use a site located on top of a simple geoelectrical area and it is particularly strongly recommended not to use a site on top of a strong anomaly.

All of these advantages incentivise the use of $\boldsymbol{H}$ and $\boldsymbol{T}$ responses as complements $\boldsymbol{Z}$ or $\boldsymbol{Z}_o$ responses, in particular when characterizing the subsurface beneath a MT profile in a 3-D environment. This supports the possibility of high-resolution studies in 3-D environments without expending large amounts of economical and computational resources, and also opening the door for the achievement of targets with high electrical resistivity values.

ACKNOWLEDGEMENTS

We would like to acknowledge the financial support to JC and XO from the IRECCSEM project (www.ireccsem.ie) funded by a Science Foundation of Ireland Investigator Project Award (SFI: 12/IP/1313) to AGJ. We would also like to acknowledge the financial support to JV from the Program SASPRO, grant 1497/03/01. Gary Egbert, Anna Kelbert and Naser Meqbel are very gratefully thanked for making their ModEM code available to the community. The authors wish to acknowledge Irish Centre for High-End Computing (ICHEC) for the computing facilities provided. Finally, the authors would like to thank Stephan Thiel, the two anonymous reviewers, and the Associate Editors Mark Everett and Ute Weckmann for their very helpful suggestions and comments on our submitted versions that improved our final paper.

REFERENCES

Avdeev, D.B. & Avdeeva, A., 2009. 3D magnetotelluric inversion using a limited-memory quasi-Newton optimization, *Geophysics,* **74**(3), F45–F57.

Baba, K., Chave, A.D., Evans, R.L., Hirth, G. & Mackie, R.L., 2006. Mantle dynamics beneath the East Pacific Rise at 17S: insights from the Mantle Electomagnetic and Tomography (MELT) experiment, *J. geophys. Res.,* **111,** B02101, doi:10.1029/2004JB003598.

Bedrosian, P.A., 2007. MT+, Integrating magnetotellurics to determine earth structure, physical state, and processes, *Surv. Geophys.,* **28,** 121–167.

Berdichevsky, M.N., Dmitriev, V. & Pozdnjakova, E.E., 1998. On two-dimensional interpretation of magnetotelluric soundings, *Geophys. J. Int.,* **133,** 585–606.

Berdichevsky, M.N. *et al.*, 2010b. Geoelectric section of the Central Tien Shan: analysis of magnetotelluric and magnetovariational responses along the Naryn Geotransverse, *Phys. Solid Earth,* **46**(8), 679–697.

Berdichevsky, M.N. & Dmitriev, V.I., 2008. *Models and Methods of Magnetotellurics,* Springer-Verlag.

Berdichevsky, M.N., Golubtsova, N.S., Varentsov, Iv.M., Pushkarev, P.Yu., Rybin, A.K. & Sokolova, E.Yu., 2010a. Geoelectric section of the Central Tien Shan: Sequential inversion of the magnetovariational and magnetotelluric data along the Naryn Line, *Phys. Solid Earth,* **46**(8), 698–706.

Booker, J.R., 2014. The magnetotelluric phase tensor: a critical review, *Surv. Geophys.,* **35,** 7–40.

Brasse, H., Lezaeta, P., Rath, V., Schwalenberg, K., Soyer, W. & Haak, V., 2002. The Bolivian Altiplano conductivity anomaly, *J. geophys. Res.,* **107**(B5), 2096, doi:10.1029/2001JB000391.

Caldwell, G.T., Bibby, H.M. & Brown, C., 2004. The magnetotelluric phase tensor, *Geophys. J. Int.,* **158,** 457–469

Campanyà, J., Ledo, J., Queralt, P., Marcuello, A. & Jones, A.G., 2014. A new methodology to estimate magnetotelluric (MT) tensor relationships: Estimation of Local transfer-functIons by Combining Interstation Transfer-functions (ELICIT), *Geophy. J. Int.,* **198,** 484–494.

Campanyà, J., Ledo, J., Queralt, P., Marcuello, A., Liesa, M. & Muñoz, J.A., 2011. Lithospheric characterization of the Central Pyrenees based on new magnetotelluric data, *Terra Nova,* **23,** 213–219.

Campanyà, J., Ledo, J., Queralt, P., Marcuello, A., Liesa, M. & Muñoz, J.A., 2012. New geoelectrical characterization of a continental collision zone in the West- Central Pyrenees: constraints from long period and broadband magnetotellurics, *Earth planet. Sci. Lett.,* **333–334,** 112–121.

Chave, A.D. & Jones, A.G., 1997. Electric and magnetic field galvanic distortion decomposition of BC87 data, *J. Geomag. Geoelectr.,* **49,** 767–789.

Chave, A.D. & Jones, A.G., 2012. *The Magnetotelluric Method,* Cambridge Univ. Press.

Chave, A.D. & Smith, J.T., 1994. On electric and magnetic galvanic distortion tensor decompositions, *J. geophys. Res.,* **99,** 4669–4682.

Dong, H. *et al.*, 2014. Three-dimensional electrical structure of the crust and upper mantle in Ordos Block and adjacent area: evidence of regional lithospheric modifications, *Geochem. Geophys. Geosyst.,* **15,** 2414–2425.

Egbert, G.D. & Kelbert, A., 2012. Computational recipes for electromagnetic inverse problems, *Geophys. J. Int.,* **189**(1), 251–267.

Falgàs, E., Ledo, J., Marcuello, A. & Queralt, P., 2009. Monitoring freshwater-seawater interface dynamics with audiomagnetotellurics data, *Near Surf. Geophys.,* **7**(5–6), 391–399.

Farquharson, C., Oldenburg, D., Haber, E. & Shekhtman, R., 2002. An algorithm for the three-dimensional inversion of magnetotelluric data, in *SEG Technical Program Expanded Abstracts,* Society of Exploration Geophysicists.

Gabàs, A. & Marcuello, A., 2003. The relative influence of different types of magnetotelluric data on joint inversions, *Earth, Planets and Space,* **55** (5), 243–248.

Grayver, A.V., 2015. Parallel three-dimensional magnetotelluric inversion using adaptive finite-element method. Part I: Theory and synthetic study, *Geophysical J. Int.,* **202,** 584–603.

Habibian, B.D. & Oskooi, B., 2014. A resolution comparison of horizontal and vertical magnetic transfer functions, *J. Earth Space Phys.,* **40**(3), 47–53.

Habibian, B.D., Brasse, H., Oskooi, B., Ernst, T., Sokolova, E. & Varentsov, Iv. & EMTESZ Working Group, 2010. The conductivity structures across the Trans-European Suture Zone from magnetotelluric and magnetovariational data modeling, *Phys. Earth planet. Inter.,* **183,** 377–386.

Heinson, G.S., Direen, N.G. & Gill, R.M., 2006. Magnetotelluric evidence for a deep crustal mineralizing system beneath the Olympic Dam iron oxide copper-gold deposit, southern Australia, *Geology,* **34**, 573–576.

Heinson, G.S., Constable, S.C. & White, A., 2000. Episodic melt transport at mid-ocean ridges inferred from magnetotelluric sounding, *Geophy. Res. Lett.,* **27,** 2317–2320.

Jones, A.G., 1983. The problem of current channelling: a critical review, *Surv. Geophys.,* **6,** 79–122.

Jones, A.G., 1986. Parkinson's pointers' potential perfidy!, *Geophys. J. R. astr. Soc.,* **87,** 1215–1224.

Jones, A.G., 1999. Imaging the continental upper mantle using electromagnetic methods, *Lithos,* **48,** 57–80.

Jones, A.G., 2012. Distortion of magnetotelluric data: its identification and removal, in *The Magnetotelluric Method: Theory and Practice*, eds Chave, A.D. & Jones, A.G., Cambridge Univ. Press.

Jones, A.G. & Garcia, X., 2003. Okak Bay AMT data-set case study: lessons in dimensionality and scale, *Geophysics,* **68,** 70–91.

Jones, A.G. *et al.*, 2009. Area selection for diamonds using magnetotellurics: Examples from southern Africa, *Lithos,* **112**(Suppl 1), 83–92.

Kelbert, A., Meqbel, N., Egbert, G.D. & Tandon, K., 2014. ModEM: a modular system for inversion of electromagnetic geophysical data, *Comput. Geosci.,* **66,** 40–53.

Kiyan, D., Jones, A.G. & Vozar, J., 2014. The inability of magnetotelluric off-diagonal impedance tensor elements to sense oblique conductors in 3-D inversion, *Geophys. J. Int.,* **196,** 1351–1364.

Kühn, C., Küster, J. & Brasse, H., 2014. Three-dimensional inversion of magnetotelluric data from Central Andean continental margin, *Earth, Planets and Space,* **66,** 112.

La Terra, E.F. & Menezes, P.T.L., 2012. Audio-magnetotelluric 3D imaging of the Regis kimberlite pipe, Minas Gerais, Brazil, *J. Appl. Geophys.,* **77,** 30–38.

Le Pape, F., Jones, A.G., Vozar, J. & Wenbo, W., 2012. Penetration of crustal melt beyond the Kunlun Fault into northern Tibet, *Nat. Geosci.,* **5,** 330–335.

Ledo, J., 2005. 2-D versus 3-D magnetotelluric data interpretation, *Surv. Geophys.,* **26,** 511–543.

Ledo, J., Queralt, P., Marti, A. & Jones, A.G., 2002. Two-dimensional interpretation of three-dimensional magnetotelluric data: an example of limitations and resolution, *Geophys. J. Int.,* **150,** 127–139.

Ledo, J., Jones, A.G., Siniscalchi, A., Campanyà, J., Kiyan, D., Romano, G. & Rouai, M. & TopoMed MT Team, 2011. Electrical signature of modern and ancient tectonic processes in the crust of the Atlas mountains of Morocco, *Phys. Earth planet. Inter.,* **185,** 82–88.

Lezaeta, P. & Haak, V., 2003. Beyond magnetotelluric decomposition: induction, current channelling, and magnetotelluric phases over 90, *J. geophys. Res.,* **108**(B6), 2305, doi:10.1029/2001JB000990.

Marcuello, A., Queralt, P. & Ledo, J., 2005. Applications of dispersion relations to the geomagnetic transfer function, *Phys. Earth planet. Inter.,* **150,** 85–91.

Meqbel, N.M, Egbert, G.D., Wannamaker, P.E., Kelbert, A. & Schultz, A., 2014. Deep electrical resistivity structure of the northwestern U.S. derived from 3-D inversion of USArray magnetotelluric data, *Earth planet. Sci. Lett.,* **402,** 290–304.

Miensopust, M.P., Queralt, P. & Jones, A.G. & the 3D MT Modellers, 2013. Magnetotelluric 3D inversion – a review of two successful workshops on forward and inversion code testing and comparison, *Geophys. J. Int.,* **193,** 1216–1238.

Muñoz, G., 2014. Exploring for geothermal resources with electromagnetic methods, *Surv. Geophys.,* **35** (1), 101–122.

Ogaya, X., Ledo, J., Queralt, P., Marcuello, A. & Quintà, A., 2013. First geoelectrical image of the subsurface of the Hontomín site (Spain) for CO_2 geological storage: a magnetotelluric 2D characterization, *Int. J. Greehouse Gas Control,* **13,** 168–179.

Ogaya, X., Queralt, P., Ledo, J., Marcuello, A. & Jones, A.G., 2014. Geoelectrical baseline model of the subsurface of the Hontomin site (Spain) for CO_2 geological storage in a deep saline aquifer: a 3D magnetotelluric characterization, *Int. J. Greehouse Gas Control,* **27,** 120–138.

Park, S.K. & Mackie, R.L., 2000. Resistive (dry?) lower crust in an active orogen, Nanga Parbat, northern Pakistan, *Tectonophysics,* **316**, 359–380.

Piña-Varas, P., Ledo, J., Queralt, P., Marcuello, A., Bellmunt, F., Hidalgo, R. & Messeiller, M., 2014. 3-D magnetotelluric exploration of Tenerife geothermal system (Canary Islands, Spain), *Surv. Geophys.,* **35**(4), 1045–1064.

Rao, C.K., Jones, A.G., Moorkamp, M. & Weckmann, U., 2014. Implications for the lithospheric geometry of the Iapetus suture beneath Ireland based on electrical resistivity models from deep-probing magnetotellurics, *Geophys. J. Int.,* **198,** 737–759.

Rosell, O., Martí, A., Marcuello, À., Ledo, J., Queralt, P., Roca, E. & Campanyà, J., 2011. Deep electrical resistivity structure of the northern Gibraltar Arc (western Mediterranean): evidence of lithospheric slab break-off, *Terra Nova*. **23,** 179–186.

Sasaki, Y., 2004. Three-dimensional inversion of static-shifted magnetotelluric data, *Earth Planets and Space,* **56,** 239–248.

Sasaki, Y. & Meju, M.A., 2006. Three-dimensional joint inversion for magnetotelluric resistivity and static shift distributions in complex media, *J. geophys. Res.,* **111**(B5), B05101, doi:10.1029/2005JB004009.

Schmucker, U., 1970. Anomalies of geomagnetic variations in the Southwestern United States, *J Geomagnet. Geoelectr.,* **15**, 193–221.

Seama, N., Baba, K., Utada, H., Toh, H., Tada, N., Ichiki, M. & Matsuno, T., 2007. 1-D electrical conductivity structure beneath the Philippine Sea: Results from an ocean bottom magnetotelluric survey, *Phys. Earth planet. Inter.,* **162,** 2–12.

Simpson, F. & Bahr, K., 2005. *Practical Magnetotellurics,* Cambridge Univ. Press.

Siripunvaraporn, W. & Egbert, G., 2009. WSINV3DMT: vertical magnetic field transfer function inversion and parallel implementation, *Phys. Earth planet. Inter.,* **173,** 317–329.

Siripunvaraporn, W., Egbert, G., Lenbury, Y. & Uyeshima, M., 2005a. Three-dimensional magnetotelluric inversion: data-space method, *Phys. Earth planet. Inter.,* **150,** 3–14.

Siripunvaraporn, W., Egbert, G. & Uyeshima, M., 2005b. Interpretation of two-dimensional magnetotelluric profile data with three-dimensional inversion: synthetic examples, *Geophys. J. Int.,* **160,** 804–814.

Soyer, W., 2002. Analysis of geomagnetic variations in the Central and Southern Andes, *PhD thesis,* Freie Universität Berlin, Fachbereich Geowissenschaften, Berlin.

Soyer, W. & Brasse, H., 2001. A magneto-variational array study in the Central Andes of N Chile and SW Bolivia, *Geophys. Res. Lett.,* **28,** 3023–3026.

Thiel, S., Heinson, G., Gray, D.R. & Gregory, R.T., 2009. Ophiolite emplacement in NE Oman: constraints from magnetotelluric sounding, *Geophys. J. Int.,* **176**(3), 753–766.

Tietze, K. & Ritter, O., 2013. Three-dimensional magnetotelluric inversion in practice-the electrical conductivity structure of the San Andreas Fault in Central California, *Geophys. J. Int.,* **195,** 130–147.

Tuncer, V.M., Unsworth, E.M. & Pana, D., 2009. Deep electrical structure of northern Alberta (Canada): implications for diamond exploration, *Can. J. Earth Sci.,* **46,** 139–154.

Unsworth, M.J., 2005. New developments in conventional hydrocarbon exploration with EM methods, in *CSEG Recorder,* April, 34–38.

Usui, Y., 2015. 3-D inversion of magnetotelluric data using unstructured tetrahedral elements: applicability to data affected by topography, *Geophys. J. Int.,* **202,** 828–849.

Varentsov, Iv.M., 2015a. Methods of joint robust inversion in MT and MV studies with application to synthetic datasets, in *Electromagnetic Sounding of the Earth's Interior: Theory, Modeling, Practice*, pp. 191–229, ed. Spichak, V.V., Elsevier.

Varentsov, Iv.M., 2015b. Arrays of simultaneous EM soundings: design, data processing, analysis, and inversion, in *Electromagnetic Sounding of the Earth's Interior: Theory, Modeling, Practice*, pp. 271–299, ed. Spichak, V.V., Elsevier.

Vozoff, K., 1991. The magnetotelluric method, in Electromagneitc Methods in Applied Geophysics – Applications, Chapter 8, pp. 641–712, ed. Nabighian, M.N., Society of Exploration Geophysicists.

Wanamaker, P.E., Hohmann, G.W. & Ward, S.H., 1984. Magnetotelluric responses of three-dimensional bodies in layered earths, *Geophysics,* **49,** 1517–1533.

Yang, B., Egbert, G.D., Kelbert, A. & Meqbel, N., 2015. Three-dimensional electrical resistivity of the north-central USA from EarthScope long period magnetotelluric data, *Earth planet. Sci. Lett.,* **422,** 87–93.

SUPPORTING INFORMATION

Additional Supporting Information may be found in the online version of this paper:

Figure S1. Inclusion of ***H*** responses in ModEM.

Figure S2. Differences between data and model responses divided by the assumed error for each type of inversion, component of the data, site and period in a pseudo-section format. Grey areas are periods with differences smaller than the assumed errors; red and blue areas are periods with differences larger than the assumed errors.
(http://gji.oxfordjournals.org/lookup/suppl/doi:10.1093/gji/ggw357/-/DC1).

Please note: Oxford University Press is not responsible for the content or functionality of any supporting materials supplied by the authors. Any queries (other than missing material) should be directed to the corresponding author for the paper.